

國立交通大學  
物理研究所  
碩士論文

以吸收光譜研究八面體結構中  
過渡金屬價態與自旋態

Spin configurations and valence state study of  
transition metal ions in octahedral environment by  
X-ray absorption spectroscopy

研究生：溫智匡

指導教授：林俊源 教授

中華民國一零二年七月


# Spin configurations and valence state study of transition metal ions in octahedral environment by X-ray absorption spectroscopy

student : Chih-Kuang Wen

Advisor : Dr. Jiunn-Yuan Lin

Institute of physics  
National Chiao Tung University

## Abstract



In this thesis, X-ray absorption near edge spectroscopy (XANES) was employed to study the valence and spin degree of freedom of transition metal ions in materials.

For the case of  $\text{Ni}(\text{NO}_3)_2$ , the Ni  $L$ -edge spectrum indicates divalent nickel in  $\text{Ni}(\text{NO}_3)_2$  compounds. Combined with the theoretical calculations, we confirm that the divalent nickel exhibits the high spin state ( $S=1$ ) in  $\text{Ni}(\text{NO}_3)_2$ . In the study,  $\text{NiO}$  ( $\text{Ni}^{2+}$ ,  $S=1$ ) was used as the standard sample. The spectrum shape differences between  $\text{NiO}$  and  $\text{Ni}(\text{NO}_3)_2$  come from the different local environments.

Moreover, we measured room temperature Mn  $K$ ,  $L_{2,3}$ -edge and Co  $K$ ,

$L_{2,3}$ -edge and temperature dependent Co  $L_{2,3}$ -edge XANES spectra in PrSrCoMnO<sub>6</sub> double perovskites. Our spectra show the Co<sup>3+</sup>/Mn<sup>4+</sup> ionic state in PrSrCoMnO<sub>6</sub>. With the help of theoretical calculations, we found that the crystal field in CoO<sub>6</sub> octahedral is close to the HS-LS transition boundary. The crystal structure in PrSrCoMnO<sub>6</sub> was solved at  $T=300$  K and  $T=12$  K, respectively. PrSrCoMnO<sub>6</sub> shows an unusual lattice change at low temperatures. The lattice volume and the average Mn-O bond length decrease, but the average Co-O bond length increases at low temperatures. We also find there is a close relationship between CoO<sub>6</sub> local environment and Co  $L$ -edge spectra line shape. The temperature dependent Co  $L$ -edge XAS spectra of PrSrCoMnO<sub>6</sub> obviously demonstrate the spin state variation with  $T$ , which can be described as the combination of a LS ground state and the triply degenerate HS first excited states.

## Acknowledgement

首先，在此非常感謝我的父母從小給了我一個良好的教育環境，讓我可以無後顧之憂的完成碩士學歷，並且在我挫折的時候給予我鼓勵，成為我如此強而有力的後盾，爸媽我愛你們！

非常感謝我的指導教授 林俊源老師，在兩年的碩士班期間給予我許許多多的建議、要求和鼓勵，也給予了我相當紮實的科學訓練。老師總會要求我們把所有事情做得更好再更好，以及嚴格的檢視自己，並且訓練了我們清晰的表達技巧，智匡相信這些訓練對我們來說都是終身受用的！

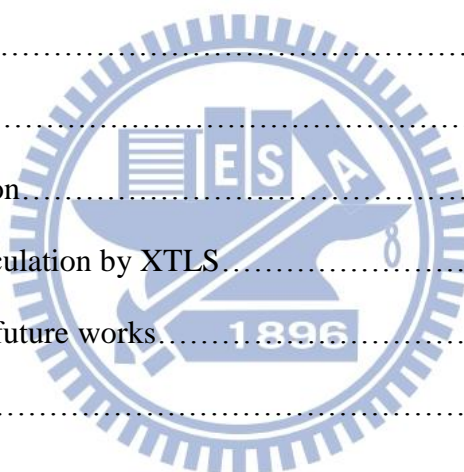
在此特別感謝國家同步輻射研究中心 陳錦明老師、胡志偉老師、林宏基老師以及李大哥、孟傑學長…等等專業的老師和學長們不厭其煩的教導和協助，我才有足夠的專業知識來完成本篇碩士論文。也很感謝實驗室的大家，小 Pa 學長、伯仲學長、CA 哥、小 P、孟恭、科科、翹屁、榜首哥、沛姍、至中、愷威、汶鑫、昶鴻、吉吉、舜鴻以及几華和包子…等等，這兩年的研究因為有你們的協助，才使得許多事情得以進行，也因為有你們大家的陪伴才讓我的碩士生涯過的如此繽紛！

最後，我要感謝我的女友相蓉，非常感謝妳自我報考研究所以來一路的陪伴支持和鼓勵！ You raise me up. To more than I can be.

## Table of contents

Abstract.....	i
Acknowledgement (Chinese).....	iii
Table of contents.....	iv
List of Figures.....	vi
List of Tables.....	ix
Chapter 1. Introduction.....	1
1-1 Motivation.....	1
1-1(a) Ni(NO <sub>3</sub> ) <sub>2</sub> .....	1
1-1(b) PrSrCoMnO <sub>6</sub> .....	2
Chapter 2. Materials Introduction.....	4
2-1(a) Introduction of Ni(NO <sub>3</sub> ) <sub>2</sub> .....	4
2-1(b) Ni(NO <sub>3</sub> ) <sub>2</sub> sample preparation.....	6
2-2(a) Introduction of PrSrCOMnO <sub>6</sub> .....	7
2-2(b) PrSrCOMnO <sub>6</sub> sample preparation.....	8
Chapter 3. Theory and Experimental Method.....	9
3-1 Theory introduction.....	9
3-1(a) Crystal Field Splitting.....	9
3-1(b) Hund's Rule.....	10
3-1(c) Jahn-Teller distortion (JT) .....	10
3-2 Experimental Method.....	11
3-2-1(a) Principle of XANES.....	12
3-2-1(b) NSRRC BL.20A H-SGM beamline equipment.....	14
3-2-1(c) NSRRC BL.17C equipment.....	15
3-2-2 X-ray diffraction.....	15
3-2-2(a) Bragg diffraction.....	15

3-2-2(b) XRD experiments.....	15
3-2-2(c) Rietveld refinement.....	16
3-3 Theoretical calculation in XTLS.....	17
Chapter 4. Results and discussion on Ni(NO <sub>3</sub> ) <sub>2</sub> .....	19
4-1 Experimental Design.....	19
4-2 Ni <i>L</i> -edge XANES spectra.....	21
4-3 XANES theoretical calculation by XTLS.....	24
4-4 Conclusions of Ni(NO <sub>3</sub> ) <sub>2</sub> .....	27
Chapter 5. Results and discussion on PrSrCoMnO <sub>6</sub> .....	28
5-1 Experimental Design.....	28
5-2 Mn XANES spectra.....	28
5-3 Co XANES spectra.....	30
5-4 Powder X-ray diffraction.....	34
5-5 XANES theoretical calculation by XTLS.....	42
Chapter 6. Conclusions and future works.....	50
Reference.....	51



## List of Figures

Fig. 2-1. The upper panel represents fragment of the crystal structure of Ni(NO <sub>3</sub> ) <sub>2</sub> in the ab – plane. The Ni <sub>1</sub> and Ni <sub>2</sub> ions are shown in octahedral oxygen environment, the nitrate groups are shown by triangulars. The Ni <sub>1</sub> form kagome – type layers while Ni <sub>2</sub> ions occupy hexagonal cavities in it. The lower panel represents the in and inter layers exchange interactions.....	5
Fig. 2-2 Magnetic susceptibility measurement of Ni(NO <sub>3</sub> ) <sub>2</sub> .....	5
Fig. 2-3 Specific heat measurement of Ni(NO <sub>3</sub> ) <sub>2</sub> .....	6
Fig. 2-4 Magnetization measurement of Ni(NO <sub>3</sub> ) <sub>2</sub> At 2 K under magnetic field.....	6
Fig. 2-5 Double perovskite structure of LaCaMnCoO <sub>6</sub> .....	7
Fig. 2-6 Temperature dependence of mass magnetization of LaSrMnCoO <sub>6</sub> measured under a magnetic field of 10 kOe in ZFC and FC conditions.....	8
Fig. 2-7 Temperature dependence of inverse magnetic molar susceptibility of LaSrMnCoO <sub>6</sub> measured under a magnetic field of 10 kOe. The line through the high temperature data points represent a fit to the Curie–Weiss law.....	8
Fig. 3-1 Crystal Field Splitting in octahedral symmetry.....	9
Fig. 3-2 Jahn-Teller distortion.....	11
Fig. 3-3 XANES of Mn <i>K</i> -edge.....	12
Fig. 3-4 Photoabsorption of an x-ray into a core level followed by photoelectron emission, filling of the core hole by an electron in another level, accompanied by fluorescence photon.....	13
Fig. 3-5 NSRRC BL.20A H-SGM beamline equipment.....	14
Fig. 3-6 NSRRC BL.17C equipment.....	15
Fig. 3-7 Input file of XTLS software. ....	17
Fig. 3-8 Initial and final electronic states setting in XTLS.....	18

Fig. 3-9 Detailed information of each states given by XTLS.....	18
Fig. 4-1 Crystal structure of NiO and Ni(NO <sub>3</sub> ) <sub>2</sub> . ....	20
Fig. 4-2 High spin and low spin in Ni <sup>2+</sup> (3d <sup>8</sup> ) case. ....	21
Fig. 4-3 Nickel L <sub>2,3</sub> edge XAS data in TEY. ....	22
Fig. 4-4 Ni 2p XAS spectra from J.-S. Kang et al. ....	23
Fig. 4-5 Ni <sup>2+</sup> XAS simulation from J.-S. Kang et al. (2007).....	23
Fig. 4-6 Ni <sup>2+</sup> HS-LS mixed XAS spectra.....	24
Fig. 4-7 Nickel L <sub>2,3</sub> edge XAS data with ligand field model calculations.....	26
Fig. 4-8 Nickel L <sub>2,3</sub> edge XAS data with free ion model calculations.....	26
Fig. 4-9. Magnetization measurement of Ni(NO <sub>3</sub> ) <sub>2</sub> At 2 K under magnetic field.....	27
Fig. 5-1 Mn L-edge XAS data in TEY mode.....	29
Fig. 5-2 Mn K-edge XAS data in transmission mode.....	29
Fig. 5-3 Co K-edge XAS spectra in transmission mode.....	30
Fig. 5-4 Co L-edge XAS data.....	32
Fig. 5-5 Co L-edge XAS spectra from reference.....	32
Fig. 5-6 Co L-edge XAS spectra from reference.....	32
Fig. 5-5 Temperature dependent Co L-edge XAS spectra on PrSrCoMnO <sub>6</sub> sample.....	33
Fig.5-9 X-ray diffraction data of powder PrSrCoMnO <sub>6</sub> sample.....	36
Fig.5-9 (a,b,c,d) Details of X-ray diffraction data and simulations on PrSrCoMnO <sub>6</sub> .....	36
Fig.5-10 Solved crystal structure of PrSrCoMnO <sub>6</sub> at T=300 K.....	37
Fig. 5-8. High spin and low spin in Ni <sup>2+</sup> (3d <sup>8</sup> ) case.....	39
Fig.5-12 X-ray diffraction data of powder PrSrCoMnO <sub>6</sub> sample at T=12K.....	40
Fig.5-13 (a,b,c,d) Details of X-ray diffraction data and simulations on PrSrCoMnO <sub>6</sub> .....	40
Fig.5-14 Solved crystal structure of PrSrCoMnO <sub>6</sub> at T=12 K.....	41
Fig. 5-15 Co L-edge XAS spectra with Co <sup>2+</sup> impurities.....	43
Fig. 5-16 Co L-edge XAS spectra with theoretical calculation.....	43

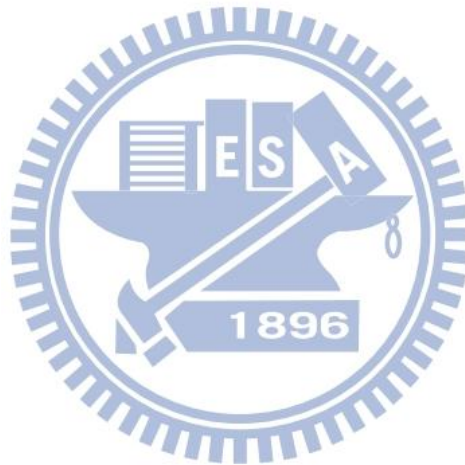


Fig. 5-17 The ground state of simulations in different $10Dq$ .....	44
Fig. 5-18 Co <i>L</i> -edge XAS in $\text{LaCoO}_3$ from M.W.Haverkort et al.....	45
Fig 5-19 Temperature dependent $\text{Co}^{3+}$ <i>L</i> -edge XAS spectra. ....	47
Fig 5-20 Co <i>L</i> -edge XAS experiment data with theoretical calculation (setting the temperature parameter equals to real experiment conditoin).....	47
Fig. 5-21 Co <i>L</i> -edge XAS spectra with theoretical calculation.....	48
Fig. 5-22 The relationship between the fitting parameter $10Dq$ with the average Co-O bond length in different $\text{Co}^{3+}$ samples.....	49



## List of Tables

Table 5-1. TM-O bond length of two <i>TM</i> sites.....	37
Table 5-2. Mn-O bond length in MnO <sub>6</sub> coordination.....	38
Table 5-3. Mn-O bond length in double perovskite samples.....	38
Table 5-4. Co-O bond length in CoO <sub>6</sub> coordination.....	38
Table.5-5 Lattice parameters of PrSrCoMnO <sub>6</sub> in T=300 K and T=12 K.....	41
Table 5-6 Energy and total spin $S(S+1)$ for each state in $10Dq=0.495$ eV by XTLS.....	44
Table 5-7 The comparison of average Co-O bond length with the fitting parameter.....	49



## Chapter 1. Introduction

The 3d transition metal (TM) exhibit varied degree of freedom in TM oxides, such as valence states and spin states. The class of TM compounds shows an enormous richness of physical properties, such as metal-insulator (MI) transitions, super-conductivity, colossal magneto-resistance (CMR), and the ordering of spin, charge, and orbitals. Many properties come from the different electronic occupation in TM 3d orbitals, e.g. different valence states coexist in the material may changes the electronic properties[Alexander N. VASILIEV], and the spin state transition may changes the magnetic properties[M.W. Haverkort]. Knowing the occupation of TM 3d orbitals would help to interpret the origin of physical properties. To study the electronic occupation of TM ions in material, we did experiments by using X-ray absorption spectroscopy. XAS is a powerful tool to study the electronic states of outer electrons, especially the TM  $L_{2,3}$ -edge XAS ( $2p \rightarrow 3d$  transition), which probe directly the valence electrons.

### 1-1 Motivation

#### 1-1(a) Ni(NO<sub>3</sub>)<sub>2</sub>

Many structure-related chemistry properties in anhydrous nitrates of divalent cations (Ba, Sr and Pb) are well studied in 1980s, which are not hygroscopic. The anhydrous nitrates of divalent elements with smaller ionic radii are very hygroscopic and are more difficult to investigate, such as Mn, Co and Ni. The crystal structure of nickel (II) nitrate, Ni(NO<sub>3</sub>)<sub>2</sub> was recently defined by G. Giester (2008) to have a rhombohedral  $R\bar{3}$  space group ( $a = 10.3569(1) \text{ \AA}$ ,  $c = 12.6761(1) \text{ \AA}$ ,  $Z = 12$ ), which shows two different sites for Ni<sup>2+</sup> ions with the ratio Ni-1 : Ni-2 = 3 : 1 [1,2]. Two nickel sites have different distorted NiO<sub>6</sub> octahedral local environments. In a distorted

NiO<sub>6</sub> octahedral environment, Ni<sup>2+</sup> ions (3d<sup>8</sup>) may exhibit either low-spin (LS, S=0) or high-spin (HS, S=1) states depending on the ratio between Hund's coupling J<sub>H</sub> and Δe<sub>g</sub> splitting. HS state would be ground state in a small distorted case.

O. Volkova et al. measured the magnetization and specific heat on Ni(NO<sub>3</sub>)<sub>2</sub> and indicate that Ni(NO<sub>3</sub>)<sub>2</sub> orders ferromagnetically at T<sub>C</sub> = 5.5 K ± 0.25 K, but the magnetic entropy released below T<sub>C</sub> amounts approximately half of the expected value Rln3 for Ni<sup>2+</sup> spin S = 1. At 2 K under magnetic field the magnetization curve of Ni(NO<sub>3</sub>)<sub>2</sub> demonstrates the saturation magnetization about 1.5 μ<sub>B</sub>/f.u. The obtained value of saturation moment amounts quite accurate 3/4 from the theoretical one M<sub>S</sub> = ngSμ<sub>B</sub> = 2.15 μ<sub>B</sub>/f.u. for Ni<sup>2+</sup>, S=1. [2] To confirm the spin state of nickel ions and whether a quarter of nickel ions show low spin state (LS, S=0) at the Ni-2 site, we measured the X-ray absorption near edge structure (XANES) on nickel L<sub>2,3</sub> edge in powder Ni(NO<sub>3</sub>)<sub>2</sub> sample and NiO single crystal as a reference.

### 1-1(b) PrSrCoMnO<sub>6</sub>

The class of cobalt-oxide based materials has attracted considerable interest in the last two decades because of expectations that spectacular properties may be found similar to those in the manganites and cuprates. e.g. Giant magnetoresistance effects have been observed in the La<sub>1-x</sub>A<sub>x</sub>CoO<sub>3</sub> (A=Ca, Sr, Ba) perovskites. A key point of cobalt oxides is that the Co<sup>3+/III</sup> ion has high degree of freedom in spin state than manganese and copper. In perovskite structure (CoO<sub>6</sub> octahedral coordination), depending on the ratio of the Hund's coupling and the crystal field between t<sub>2g</sub> and e<sub>g</sub> state, Co<sup>3+</sup> ions may stay in the low-spin state (3d<sup>6</sup>, S=0), intermediate-spin state (3d<sup>6</sup>, S=1) or high-spin state (3d<sup>6</sup>, S=2). Co<sup>3+</sup> is generally assumed to represent LS state in ReCoO<sub>3</sub> perovskite (Re=Eu, Sm).

Cobalt ions exhibit varied valence and spin state in double perovskites materials,

which has the general formula of  $A'A''B'B''O_6$ , where  $A'$  and  $A''$  sites are occupied by the rare earth element or Alkaline earth metal,  $B'$  and  $B''$  sites by transition metal ions. J. Androulakis [3] studied  $\text{LaSrCoMnO}_6$  sample by using XRD, magnetism and transport measurement. They assume that  $\text{LaSrCoMnO}_6$  is cubic double perovskite structure, and valence of Mn ion shows 4+, while the cobalt ion shows  $\text{Co}^{3+}$ .

We are interested in the valence and spin state of transition metal ions in different compound of double perovskites  $\text{PrSrCoMnO}_6$ . In our previous work, the Co  $K$ -edge XANES spectrum presents the trivalence cobalt in  $\text{PrSrCoMnO}_6$ , but the  $L$ -edge XANES spectrum shows a very different look with those  $\text{ReCoO}_3$  perovskite ( $\text{Re}=\text{Eu, Sm}$ )  $\text{Co}^{3+}$  LS spectra, contrarily, it's slightly similar to the spectrum of layered  $\text{Sr}_2\text{CoO}_3\text{Cl}$  compound studied by Z. Hu et al.(2004)[4]. Z. Hu et al. demonstrate that the  $\text{Co}^{3+}$  ions with the  $\text{CoO}_5$  pyramidal coordination in the layered  $\text{Sr}_2\text{CoO}_3\text{Cl}$  compound shows an unambiguously high spin state (HS,  $3d^6$ ,  $S=2$ ). In our study, we particularly reexamine the spin state of cobalt ions in  $\text{PrSrCoMnO}_6$  and expect to see  $\text{Co}^{3+}$  high spin state in perovskite structure.

## Chapter 2. Materials Introduction

### 2-1(a) Introduction of Ni(NO<sub>3</sub>)<sub>2</sub>

The crystal structure of nickel (II) nitrate, Ni(NO<sub>3</sub>)<sub>2</sub> was recently solved to have a rhombohedral  $R\bar{3}$  space group ( $a = 10.3569(1) \text{ \AA}$ ,  $c = 12.6761(1) \text{ \AA}$ ,  $Z = 12$ ), which shows two different sites for Ni<sup>2+</sup> ions with the ratio Ni-1 : Ni-2 = 3 : 1 [1,2]. Both nickel sites possess octahedral oxygen environment. Every NiO<sub>6</sub> octahedron is connected via six nitrate groups with twelve neighbouring octahedra. As shown in Fig.2-1, the Ni ions form two-dimensional Kagome lattice in the ab-plane, and Ni-2 ions occupy the hexagonal cavities. In both Ni-1 and Ni-2 positions the apical oxygen anions are shifted aside from the symmetric vertical location to 11° and 12°, respectively. In the NiO<sub>6</sub> octahedral environment, the Ni 3d degenerate state was separated into  $e_g$  and  $t_{2g}$  state with  $10Dq$  difference by the crystal field, and the  $e_g$  state was separated into  $x^2-y^2$  and  $3z^2-r^2$  with  $\Delta e_g$  difference by the distortion. Depending on the ratio between Hund's coupling  $J_H$  and  $\Delta e_g$  splitting, Ni<sup>2+</sup> ions ( $3d^8$ ) may exhibit either low-spin (LS,  $S=0$ ) or high-spin (HS,  $S=1$ ) states. HS state would be ground state in a small distorted case.

O. Volkova et al. measured the magnetization and specific heat on Ni(NO<sub>3</sub>)<sub>2</sub> and indicate that Ni(NO<sub>3</sub>)<sub>2</sub> orders ferromagnetically at  $T_C = 5.5 \text{ K} \pm 0.25 \text{ K}$  (Fig.2-2,2-3), but the magnetic entropy released below  $T_C$  amounts approximately half of the expected value  $R\ln 3$  for Ni<sup>2+</sup> spin  $S=1$ . At 2 K under magnetic field the magnetization curve of Ni(NO<sub>3</sub>)<sub>2</sub> demonstrates the saturation magnetization about  $1.5 \mu_B/\text{f.u.}$  The obtained value of saturation moment amounts quite accurate  $3/4$  from the theoretical one  $M_S = ngS\mu_B = 2.15 \mu_B/\text{f.u.}$  for Ni<sup>2+</sup>,  $S=1$  (see Fig.2-4) [2]. To confirm the spin state of nickel ions, we measured the X-ray absorption near edge structure (XANES) on nickel L<sub>2,3</sub> edge in powder Ni(NO<sub>3</sub>)<sub>2</sub> sample and NiO single crystal as a reference.

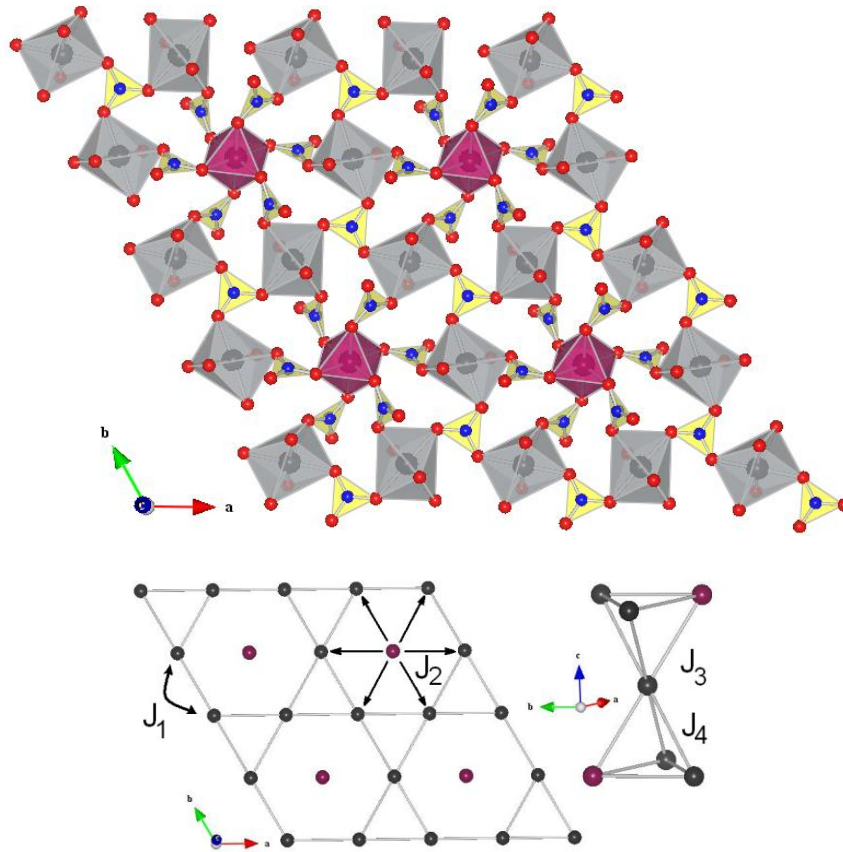


Fig. 2-1. The upper panel represents fragment of the crystal structure of  $\text{Ni}(\text{NO}_3)_2$  in the  $ab$  – plane. The  $\text{Ni}_1$  and  $\text{Ni}_2$  ions are shown in octahedral oxygen environment, the nitrate groups are shown by triangulars. The  $\text{Ni}_1$  form kagome – type layers while  $\text{Ni}_2$  ions occupy hexagonal cavities in it. The lower panel represents the in and inter layers exchange interactions. [2]

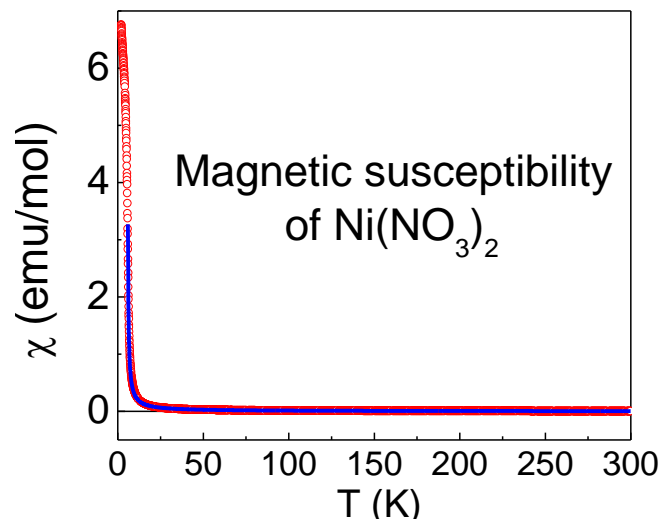


Fig. 2-2. Magnetic susceptibility measurement of  $\text{Ni}(\text{NO}_3)_2$ . [2]

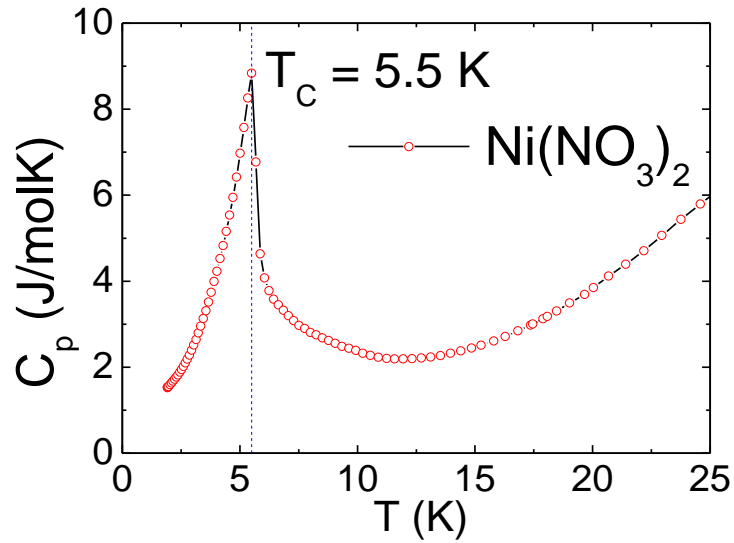


Fig. 2-3. Specific heat measurement of  $\text{Ni}(\text{NO}_3)_2$ . [2]

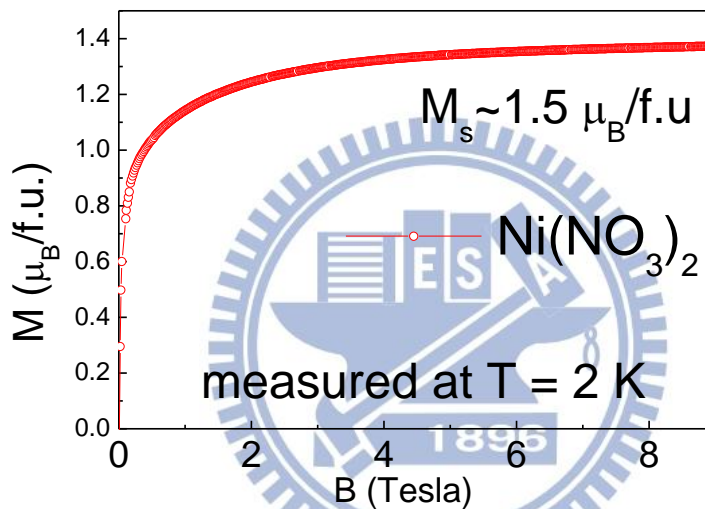


Fig. 2-4. Magnetization measurement of  $\text{Ni}(\text{NO}_3)_2$  At 2 K under magnetic field. [2]

### 2-1(b) $\text{Ni}(\text{NO}_3)_2$ sample preparation

For preparation of powder sample  $\text{Ni}(\text{NO}_3)_2$ , the glass with mixture of  $\text{Ni}(\text{NO}_3)_2 \cdot 6\text{H}_2\text{O}$  and anhydrous  $\text{HNO}_3$  were placed in a desiccator containing phosphorus pentoxide. After three weeks  $\text{Ni}(\text{NO}_3)_2$  formed as light green polycrystalline solid. [5]



## 2-2(a) Introduction of PrSrCOMnO<sub>6</sub>

Double perovskites of the general formula  $A'A''B'B''O_6$ , the crystal structure as shown in Fig.2-5,  $A'$  and  $A''$  sites are occupied by the rare earth element or Alkaline earth metal,  $B'$  and  $B''$  sites by transition metal ions. J. Androulakis [3] studied LaSrCoMnO<sub>6</sub> sample by using XRD, magnetism and transport measurement. They assume that LaSrCoMnO<sub>6</sub> is cubic double perovskite structure, and valence of Mn ion shows Mn<sup>4+</sup>, and the cobalt ion shows Co<sup>3+</sup>, which may stay in the intermediate-spin state ( $3d^6$ ,  $S=1$ ) or high-spin state ( $3d^6$ ,  $S=2$ ). Magnetization measurement shows a phase transition at  $T_c \sim 225$  K, and the samples exhibit ferromagnetic behavior with a spin-glass-like character below  $T_c$  (see Fig.2-6). The shape of the  $\chi^{-1}(T)$  curve is characteristic of ferrimagnetic behavior. For  $T > 250$  K the  $\chi^{-1}(T)$  data are fitted well to the Curie–Weiss law as shown in Fig.2-7. Since PrSrCoMnO<sub>6</sub> has a similar structure with LaSrCoMnO<sub>6</sub>, we are interested in the valence and spin state of TM ions in different rare earth element compound.

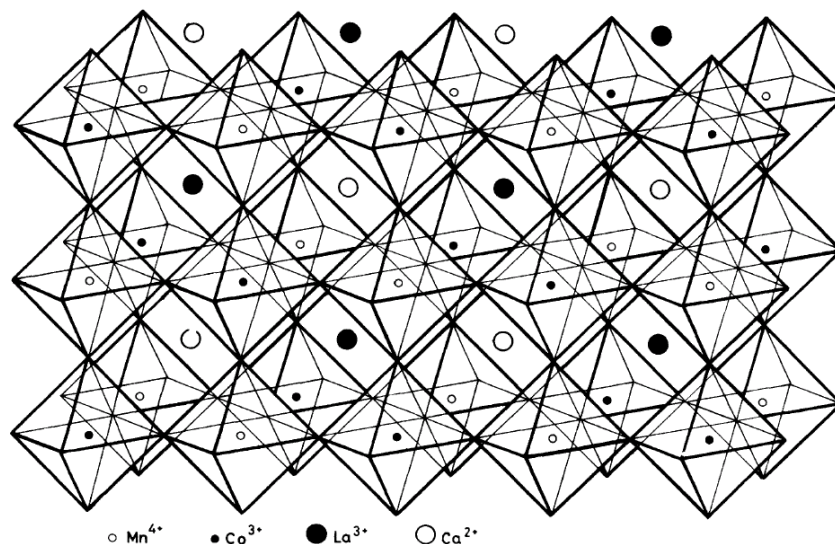


Fig. 2-5 Double perovskite structure of LaCaMnCoO<sub>6</sub>. [6]

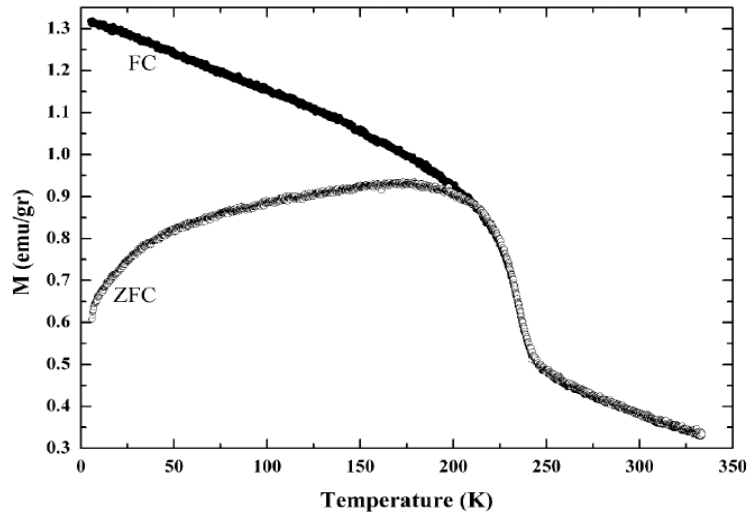


Fig. 2-6 Temperature dependence of mass magnetization of  $\text{LaSrMnCoO}_6$  measured under a magnetic field of 10 kOe in ZFC and FC conditions. [3]

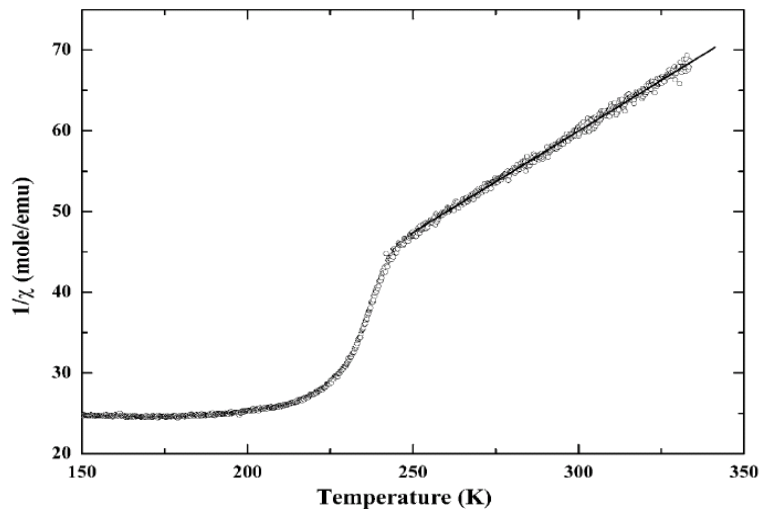


Fig. 2-7 Temperature dependence of inverse magnetic molar susceptibility of  $\text{LaSrMnCoO}_6$  measured under a magnetic field of 10 kOe. The line through the high temperature data points represents a fit to the Curie-Weiss law. [3]

### 2-2(b) $\text{PrSrCOMnO}_6$ sample preparation

The mass of powder  $\text{Pr}_2\text{O}_3$ ,  $\text{Sr}(\text{NO}_3)_2$ ,  $\text{Co}_3\text{O}_4$  and  $\text{Mn}_2\text{O}_3$  are appropriately distributed by their molecular weight and the chemical formula of  $\text{PrSrCOMnO}_6$ . The starting mixture are baked at  $T=1000^\circ\text{C}$  and sintering at  $1250\text{--}1420^\circ\text{C}$ , with subsequent cooling to room temperature at the rate of  $100^\circ\text{C/h}$ . [7]

## Chapter 3. Theory and Experimental Method

### 3-1 Theory introduction

#### 3-1(a) Crystal Field Splitting

Crystal field splitting (also called as ligand field multiplet-LFM) model is to approximate the transition metal(TM) as an isolated atom surrounded by a distribution of charges, which mimic the system, molecule, or solid, around the TM. This seems to be a very simplistic model but it was successful in explaining a large range of experiments. A TM ion in the gas phase has five degenerate  $3d$  orbitals. When the metal ion is placed in a crystal with six neighboring ions equidistant on the three axes, the crystal field is octahedral and its symmetry properties belong to the cubic group  $O_h$ . The effect of cubic crystal field is that the five  $3d$  orbitals will lose their degeneracy and split into doubly degenerate  $e_g$  state ( $3z^2-r^2$  and  $x^2-y^2$ , point directly to ligands) with a higher energy and triply degenerate  $t_{2g}$  state ( $xy, yz$  and  $zx$ , point between ligands) with a lower energy. (see Fig. 3-1)

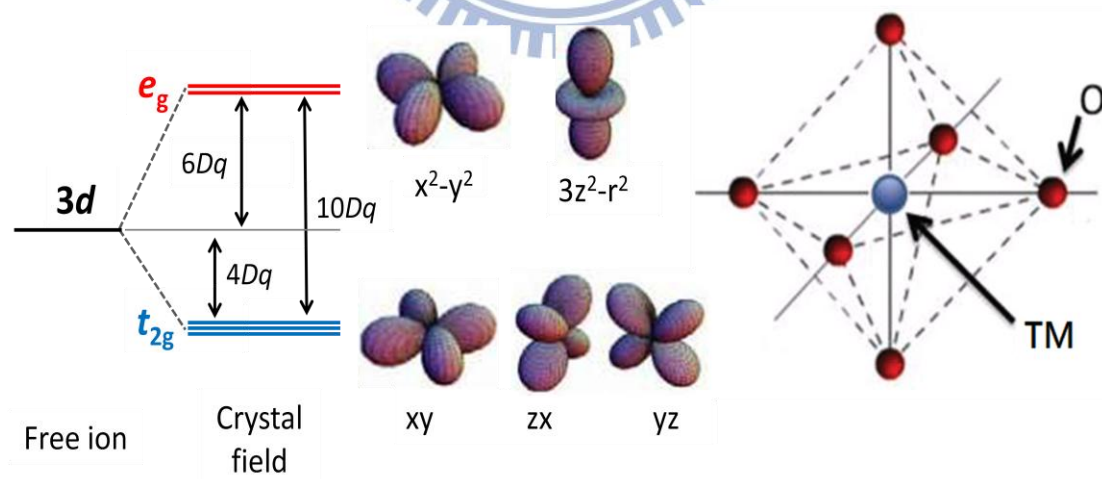


Fig. 3-1 Crystal Field Splitting in octahedral symmetry

### 3-1(b) Hund's Rule

Hund's rules was referred to a set of rules formulated by German physicist Friedrich Hund around 1927, which can be used to discuss the ground state symmetries of partly-filled 3d band in TM compounds. The three rules are :

1. For a given electron configuration, the term with the maximum value of the total spin angular momentum  $\mathbf{S}$  has the lowest energy.
2. For a given total spin angular momentum  $\mathbf{S}$ , the term with the largest value of the total orbital angular momentum  $\mathbf{L}$  has the lowest energy.
3. For a given term, in an atom with outermost subshell half-filled or less, the level with the lowest value of the total angular momentum  $\mathbf{J}$  lies lowest in energy. If the outermost shell is more than half-filled, the level with the highest value of  $\mathbf{J}$  is lowest in energy.

### 3-1(c) Jahn-Teller distortion (JT)

The Jahn–Teller distortion is named after Hermann Arthur Jahn and Edward Teller, who proved that orbital nonlinear spatially degenerate molecules cannot be stable, and will undergo a geometrical distortion that removes that degeneracy to lowers the overall energy. The JT effect is most often encountered in octahedral complexes of the TM. For example, in the  $d^9$  electronic configuration gives three electrons in the two degenerate  $e_g$  orbitals, leading to a doubly degenerate electronic ground state. Such complexes will distort along one axes (set as  $z$  axis), and breaks the degeneracy to lower the overall energy. When such an elongation occurs, the  $3z^2-r^2$  orbital will lower its energy level from the electrostatic repulsion, and cause a energy difference  $\Delta e_g$  between  $x^2-y^2$  orbital, see Fig. 3-2. The JT effect was arisen in such configurations,  $d^9$ , low-spin  $d^7$  and high-spin  $d^4$  complexes, which all have doubly degenerate ground states.

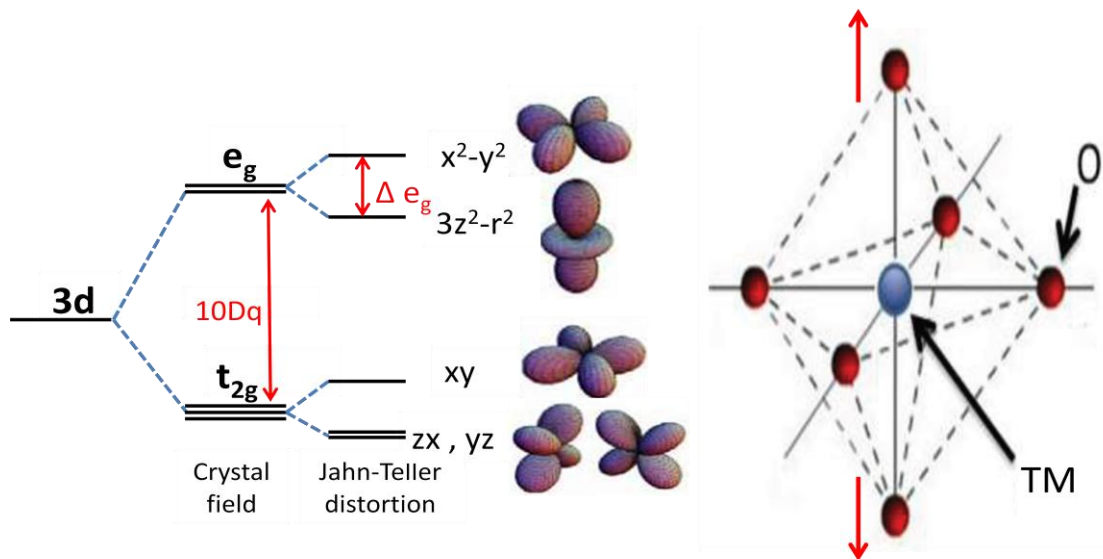


Fig. 3-2 Jahn-Teller distortion

### 3-2 Experimental Method

In the X-ray energy region, the mass photoabsorption coefficient generally decreases as the photon energy increase, but there still exist some particular raising range when the incident photon energy fortuitously satisfy the excitation and excites the core electron to outer empty shell. Depending on the energy range, X-ray is roughly separate into two parts, soft X-ray ( $h\nu < 2000$  eV, weak penetration, the experiment must be down in ultra high vacuum) and hard X-ray ( $h\nu > 2000$  eV, high penetration, the experiment can be down in the air.)

X-ray absorption spectroscopy (XAS) is a powerful tool to study the electronic states of outer electrons, the valence electron states in material. XAS can roughly separate into two regions, XANES and EXAFS. In XANES(X-ray absorption near edge structure), the edge energy increase with the increasing of elements valence in material, which come from the interaction between nucleus and outer shell electrons. This phenomenon is quite obvious in K-edge(see Fig.3-3.). In EXAFS(Extended X-ray Absorption Fine Structure ), we can get some information about the number of

atoms around and the distance between each surrounding atoms. In our studies, we focus on the XANES experiment to investigate the valence and spin state of transition metal ions in material.

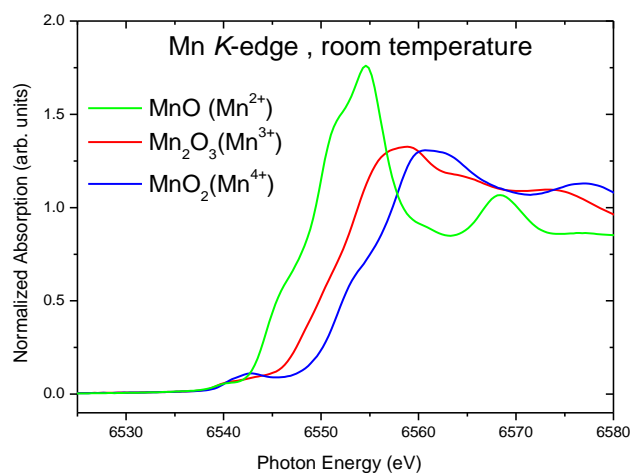


Fig. 3-3 XANES of Mn K-edge

### 3-2-1(a) Principle of XANES

In the X-ray Absorption Near Edge Structure (XANES) region, starting about 5 eV beyond the absorption threshold to around 40 eV higher. According to quantum mechanics, any electrons in the atom can be described by the principal quantum number  $n$ , orbital angular momentum  $l$ , and magnetic quantum number  $m_l$ . The electric transition obeys the dipole selection rule  $\Delta l = +1, -1$ , and  $\Delta m_l = +1, -1, 0$ . In K-edge, the core electron is excited from 1s shell to np orbital. For the  $L_1$ ,  $L_2$  and  $L_3$  absorption edge, core electrons were excited from the  $2s$ ,  $2p_{1/2}$  and  $2p_{3/2}$  orbital. The TM  $L_{2,3}$ -edge spectra can be describe as the transition from  $2p^6 3d^n$  initial state to  $2p^5 3d^{n+1}$  final state, which is extremely sensitive to the symmetry of the initial state.

There are two kind of signals in XANES, total electron yield (TEY) and X-ray fluorescence yield (FY). TEY is used to study the surface state of material. As the material absorbed the X-ray photon, the core level electron was consequently emitted

as a photoelectron. During the Coulomb interaction between the photoelectron and other electrons in the material, the photoelectron from inner material is undetectable. On the other hand, fluorescence yield is used to study the bulk state. As the absorption occurred, a core hole was created. The resulting core hole is filled by capture of an electron from another shell by emission of a fluorescent photon. Since the fluorescent photon has no Coulomb interactions with other electrons, inner material signals were obtained.

**X-ray Fluorescence:** An x-ray with energy = the difference of the core-levels is emitted.

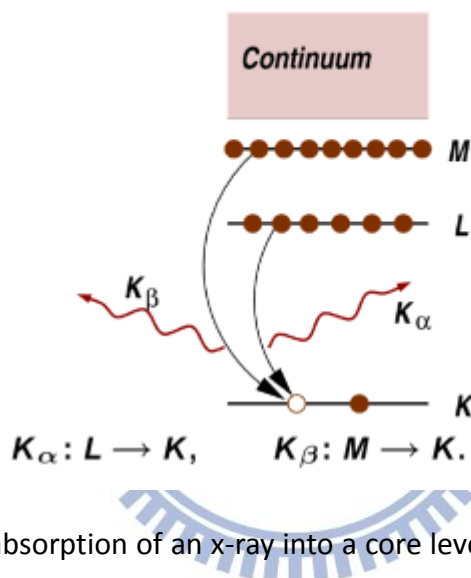
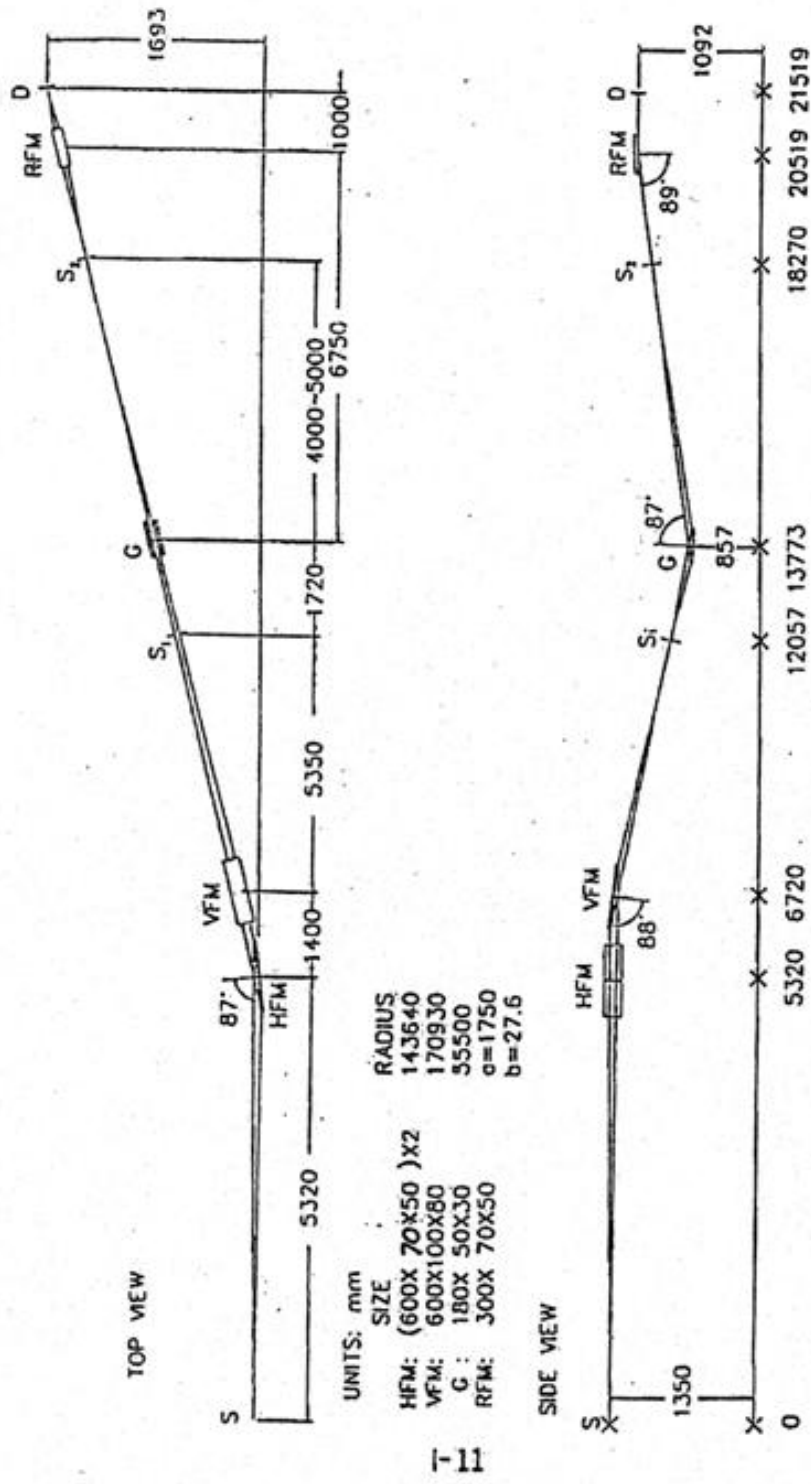


Fig. 3-4 Photoabsorption of an x-ray into a core level followed by photoelectron emission, filling of the core hole by an electron in another level, accompanied by fluorescence photon.

The XAS experiments were performed at the BL.20A H-SGM beamline, BL.11A Dragon beamline, and BL. 17C at the National Synchrotron Radiation Research Center (NSRRC) in Taiwan.

3-2-1(b) NSRRC BL.20A H-SGM beamline equipment



The sketch for the 6m HSGM (High energy Spherical Grating Monochromator), S is the source. HFM, VFM are spherical mirrors. S<sub>1</sub>, S<sub>2</sub> are respectively the entrance slit and the exit slit. G is a spherical grating. RFM is an ellipsoidal mirror. D is a sample.

Fig. 3-5 NSRRC BL.20A H-SGM beamline equipment



### 3-2-1(c) NSRRC BL.17C equipment

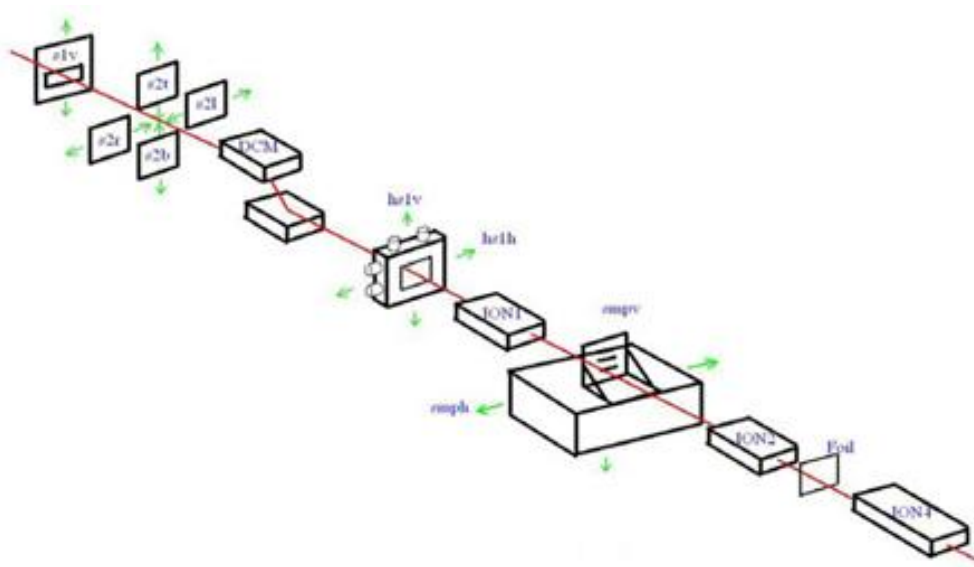


Fig. 3-6 NSRRC BL.17C equipment

### 3-2-2 X-ray diffraction

#### 3-2-2(a) Bragg diffraction

To study the crystal structure, we did experiments by using X-ray diffraction (XRD). Diffraction occurs as the incidence of X-ray to the material, according to the **Bragg's law**, Where  $d$  is the spacing between the planes in the atomic lattice,  $\theta$  is the angle between the incident ray and the scattering planes,  $n$  is an integer and  $\lambda$  is the wavelength of incident wave. e.g.  $\lambda(K\alpha_1) = 1.5406 \text{ \AA}$  for copper target.

$$2d \sin\theta = n\lambda$$

#### 3-2-2(b) XRD experiments

The  $\theta$ - $2\theta$  scans, also called normal scans, are always satisfy the Bragg's law, which the angle from incident beam to sample surface ( $\theta$ ) always keep half the angle from incident beam to detector ( $2\theta$ ).

### 3-2-2(c) Rietveld refinement

Rietveld refinement is a technique for characterizing the crystalline materials. The x-ray diffraction of powder samples results in a pattern characterised by reflections (peaks in intensity) at certain positions. The height, width and position of these reflections can be used to determine many aspects of the materials structure.

The Rietveld method, which was able to deal reliably with strongly overlapping reflections, uses a least squares approach to refine a theoretical line profile until it matches the measured profile, and Rietveld method.

Where  $W_i$  is the weight,  $W_i=1/Y_{i(obs)}$ ,  $Y_{i(obs)}$  is the real peak intensity (counts) from experiment and  $Y_{i(cal)}$  is the theory calculated peak intensity.

$$Y_{i(cal)} = \sum A_p \sum m_{hkl} LP_{|F_{hkl}|^2} \phi_p(2\theta_i - 2\theta_{hkl}) P_{hkl} + Y_{ib}$$

$P$  is Phase Number,  $A$  is Scale Factor,  $M_{hkl}$  is the multiplicity of hkl surface,  $LP$  is Lorentz-polarization factor,  $F_{hkl}$  is the Structure Factor of hkl surface,  $\phi$  is wave function,  $P_{hkl}$  is the prefer orientation function and  $Y_{ib}$  is the background signal.

In the Rietveld method, three factors can be used to determine the accuracy:

The Weighted Profile R-factor  $R_{wp} = \left\{ \sum_i W_i \left( \frac{Y_{i(obs)} - Y_{i(cal)}}{Y_{i(obs)}} \right)^2 \sum_i W_i Y_{i(obs)} \right\}^{1/2}$

The Profile R-factor  $R_p = \sum_i \left| \frac{Y_{i(obs)} - Y_{i(cal)}}{Y_{i(obs)}} \right| / \sum_i Y_{i(obs)}$

The Bragg R-factor  $R_B = R_I = \sum_i \left| \frac{I_{h(kl)} - I_{(hkl)}}{I_{h(kl)}} \right|^2 / \sum_i I_{h(kl)}$

### 3-3 Theoretical calculation in XTLS

The theoretical calculations of transition metal  $L_{2,3}$  XAS line shape is calculated by the XTLS software compiled by Dr. A. Tanaka[8], and the input file parameters were provided by Dr. Z. Hu.

In XTLS calculations, full atomic multiplet effect and ligand field multiplet effect are considered. The full atomic multiplet effect includes the  $3d-3d$  and  $2p-3d$  Coulomb and exchange interactions inside transition metal ions, while the ligand field multiplet effect includes the hybridization of transition metal  $3d$  orbital with the O  $2p$  ligands, and the local crystal field. Fig. 3-7 shows the changeable parameters in XTLS.

```
XCRD:
//XCARD for the 2pXAS on EuCoO3 oct site
(
  U3d3d = 5.5;
  U3d2p = 7.0;
  Dlt = 2.0;
  fHyb = 1.0;

  fHyb = 1.0;
  pds = 1.7000*fHyb;
  pdp = pds/2.16*fHyb;
  Vb1 = sqrt(3.0)*pds;
  Va1 = sqrt(3.0)*pds;
  Vb2 = 2*pdp;
  Ve = 2*pdp;

  Tpp=0.5;

  A0h=0.54;
  Deg=0.0;
  Dt2g=Deg/4.0;
  Ds = (Deg+Dt2g)/7.0;
  Dt = (3*Deg-4*Dt2g)/35.0;

```

2, 42 頂端

Fig. 3-7 Input file of XTLS software.

In the first part, parameter **U3d3d** and **U3d2p** represent the Coulomb and exchange interactions between  $3d-3d$  and  $2p-3d$  electrons inside transition metal ions. Parameter **Dlt** represents the charge transfer energy, in transition metal  $L_{2,3}$ -edge XAS spectra ( $2p \rightarrow 3d$ ), the transition can be describe as  $\alpha|2p^6 3d^n\rangle + \beta|2p^6 3d^{n+1} \underline{L}\rangle \rightarrow \alpha'$

$|2p^5 3d^{n+1}\rangle + \beta' |2p^5 3d^{n+2} \underline{L}\rangle$ , where  $\underline{L}$  denotes a charge transfer from ligand and create a ligand hole, and  $\Delta t$  is the energy difference between  $|2p^6 3d^n\rangle$  and  $|2p^6 3d^{n+1} \underline{L}\rangle$  state. In the second part, parameter **pds** is the hybridization coefficient between TM 3d and ligand 2p orbitals. In the third part, parameter **AO<sub>h</sub>** is the local crystal field on TMO<sub>6</sub> coordination with an octahedral symmetry, and parameter **D<sub>eg</sub>** is the energy splitting  $\Delta e_g$  from the distorted TMO<sub>6</sub> octahedral. Fig. 3-8 shows setting of the initial and final electronic states, which depend on the transition metal ions. Other parameters are mentioned in M. W. Haverkort [9]. In the calculation result, XTLS gives first 16 states spectra, including the energy and angular momentum information of each state. (see Fig. 3-9)

CNFG:			
	Ld	2p	3d
#i1	10	6	6
#i2	9	6	7
#i3	8	6	8
#f1	10	5	7
#f2	9	5	8
#f3	8	5	9

Fig. 3-8 Initial and final electronic states setting in XTLS.

```

Xtls ver. 9.0 coded by Arata Tanaka on 5th Oct. 2009
("Legacy" edition with static memory allocation)
compiled for a scalar machine
===== state #i =====
#          1      E= -7.8838113219566495
-----
Orbit #1 ==>3d      Orbit #2 ==>ld
<S_2 S_1>= -0.4838654  <L_2 L_1>= 0.7922200E-01<J_2 J_1>= -0.7304756
-----
Total moments over the orbitals specified in "Mag" command.
<S_2 S_1>= 0.2077324  <L_2 L_1>= 25.16177  <J_2 J_1>= 25.21459
===== state #i =====
#          2      E= -7.7817331049476302
-----

```

Fig. 3-9 Detailed information of each states given by XTLS.

## Chapter 4. Results and discussion on Ni(NO<sub>3</sub>)<sub>2</sub>

To study the valence and spin state of nickel ions, we measured the X-ray absorption near edge spectroscopy (XANES) at nickel  $L_{2,3}$  edge in powder Ni(NO<sub>3</sub>)<sub>2</sub> sample and NiO single crystal as a reference.

### 4-1 Experimental Design

The XAS experiments were performed at the H-SGM beamline at the National Synchrotron Radiation Research Center (NSRRC) in Taiwan. Clean sample surface were obtained by cleaving samples in chamber with pressure lower than  $10^{-7}$  mbar. Room temperature Ni  $L$ -edge XAS was recorded in total electron yield (TEY) in ultra high vacuum ( $\sim 10^{-10}$  mbar) chamber.

The crystal structure of nickel (II) nitrate, Ni(NO<sub>3</sub>)<sub>2</sub> was solved to have a rhombohedral  $R\bar{3}$  space group ( $a = 1.03569(1)$  nm,  $c = 1.26761(1)$  nm,  $Z = 12$ ), which shows two different sites for Ni<sup>2+</sup> ions with the ratio Ni-1 : Ni-2 = 3 : 1 [1]. Two nickel sites have different distorted NiO<sub>6</sub> octahedral local environments as shown in Fig.4-1. In the NiO<sub>6</sub> octahedral environment, the Ni 3d degenerate state was separated into  $e_g$  and  $t_{2g}$  state with  $10Dq$  difference by the crystal field, and the  $e_g$  state was separated into  $x^2-y^2$  and  $3z^2-r^2$  with  $\Delta e_g$  difference by the distortion. Ni<sup>2+</sup> ions ( $3d^8$ ) has six electrons in the  $t_{2g}$  state and two in the  $e_g$  state, depending on the ratio between Hund's coupling  $J_H$  and  $\Delta e_g$  splitting, it may exhibit either low-spin (LS,  $S=0$ ) or high-spin (HS,  $S=1$ ) states as shown in Fig. 4-2. An easy way to calculate the total energy of HS or LS state is to set the  $t_{2g}$  energy level to be zero, gain one crystal field energy  $10Dq$  for each electron which stays in  $e_g$  state, and also consider about the exchange interaction (Hund's coupling) between the 3d electrons.

$$E_{total} = E_{C.F} + E_{ex}$$

$$E_{ex} = -\left[\frac{n(n-1)}{2} + \frac{m(m-1)}{2}\right]J_H$$

$n$  is the number of spin up electrons,  $m$  is the number of spin down electrons,  $J_H$  is the Hund's coupling energy. For  $Ni^{2+}$ , the total energy of HS and LS can be describe as :

$$E_{HS} = 2 * 10Dq - 13J_H + \Delta e_g$$

$$E_{LS} = 2 * 10Dq - 12J_H$$

$$E_{HS} - E_{LS} = \Delta e_g - J_H$$

HS state would be ground state in a small distorted case.

The Ni  $L_{2,3}$  ( $2p \rightarrow 3d$ ) absorption spectra obeys the dipole selection rule, the transition can be describe as  $\alpha|2p^6 3d^n\rangle + \beta|2p^6 3d^{n+1} \underline{L}\rangle \rightarrow \alpha' |2p^5 3d^{n+1}\rangle + \beta' |2p^5 3d^{n+2} \underline{L}\rangle$ , where  $\underline{L}$  denotes a charge transfer from ligand to nickel. The Ni 2p core-hole spin-orbit coupling splits the spectra into two parts, namely the  $L_3$  ( $h\nu \sim 853$  eV) and  $L_2$  ( $h\nu \sim 871$  eV) white lines regions. The line shape of spectrum depends on the atomic mutiplet effect including Ni  $3d$ - $3d$  and  $2p$ - $3d$  Coulomb and exchange interactions, hybridization of Ni  $3d$  orbital with the O  $2p$  ligands, and the local crystal field.

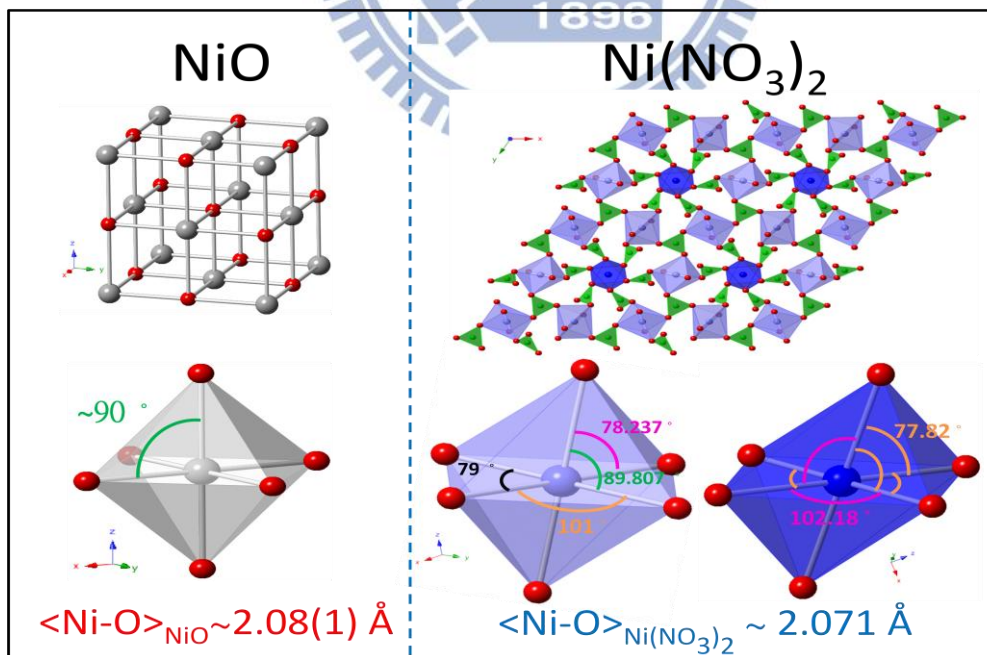


Fig. 4-1. Crystal structure of NiO and  $Ni(NO_3)_2$ .

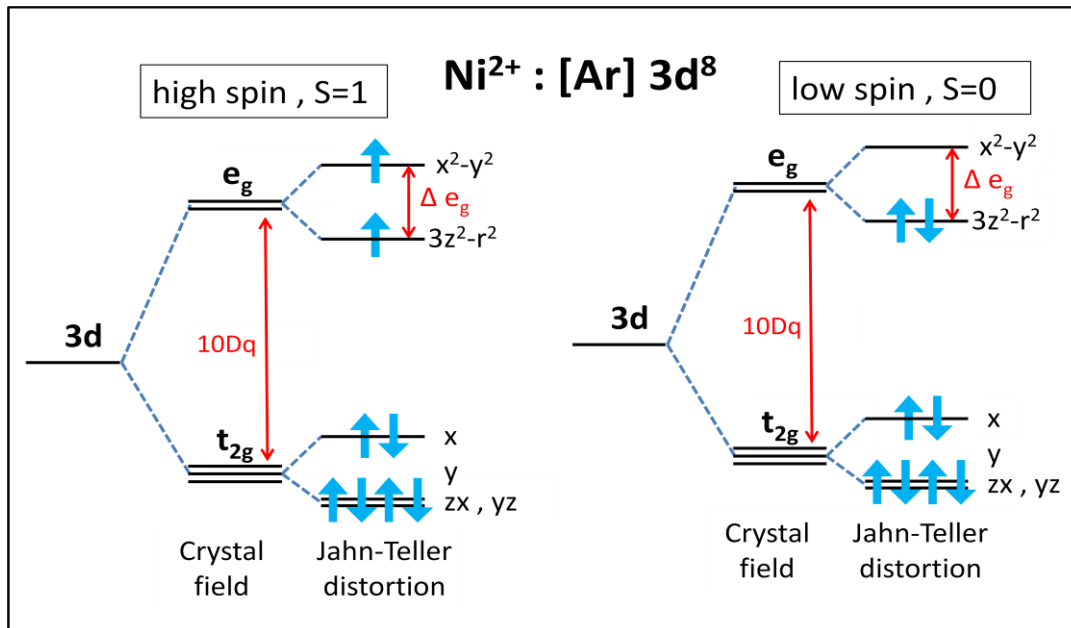


Fig. 4-2. High spin and low spin in  $\text{Ni}^{2+}$  ( $3d^8$ ) case.

#### 4-2 Ni L-edge XANES spectra

Fig. 4-3 shows the Ni  $L_{2,3}$  XAS experiment spectra of NiO and  $\text{Ni}(\text{NO}_3)_2$  taken at room temperature. NiO is generally accepted to have divalent nickel with a HS ( $S=1$ ) state as a standard sample. In the Ni  $L_3$ -edge ( $2p_{3/2} \rightarrow 3d$  transition), We found the line shape in of  $\text{Ni}(\text{NO}_3)_2$  is far away from the  $\text{Ni}^{3+}$  spectrum as shown in Fig. 4-4[10]. Both NiO and  $\text{Ni}(\text{NO}_3)_2$  spectra have a mean peak at 853.35 eV in  $L_3$ -edge, which can be used to determine the valence of nickel ions, means the nickel ions are also divalent in  $\text{Ni}(\text{NO}_3)_2$ [10,11]. At the second peak of  $L_3$ -edge,  $\text{Ni}(\text{NO}_3)_2$  has a higher intensity at 855.1 eV and more peak splitting from the mean peak than NiO. We also see a shoulder characteristic at 856.5 eV in NiO but it disappeared in  $\text{Ni}(\text{NO}_3)_2$  spectrum. These two differences come from the ligand field multiplet effect, which includes the hybridization with O  $2p$  ligands and the local crystal field from their different  $\text{NiO}_6$  environments. In the  $L_2$ -edge ( $2p_{1/2} \rightarrow 3d$ ), both spectra split into two peaks,  $\text{Ni}(\text{NO}_3)_2$  has a slightly lower intensity at 870.7eV but a visible higher intensity

at 871.8 eV than NiO. Again, these intensity differences come from the ligand field multiplet effect. The broad peak at 859 eV is the  $|2p^6 3d^9 \underline{L}\rangle \rightarrow |2p^5 3d^{10} \underline{L}\rangle$  transition from charge transfer effect, while a broad characteristic at 866.7 eV in NiO spectrum is the  $2p \rightarrow 4s$ -like transition called as continue edge jump [9].

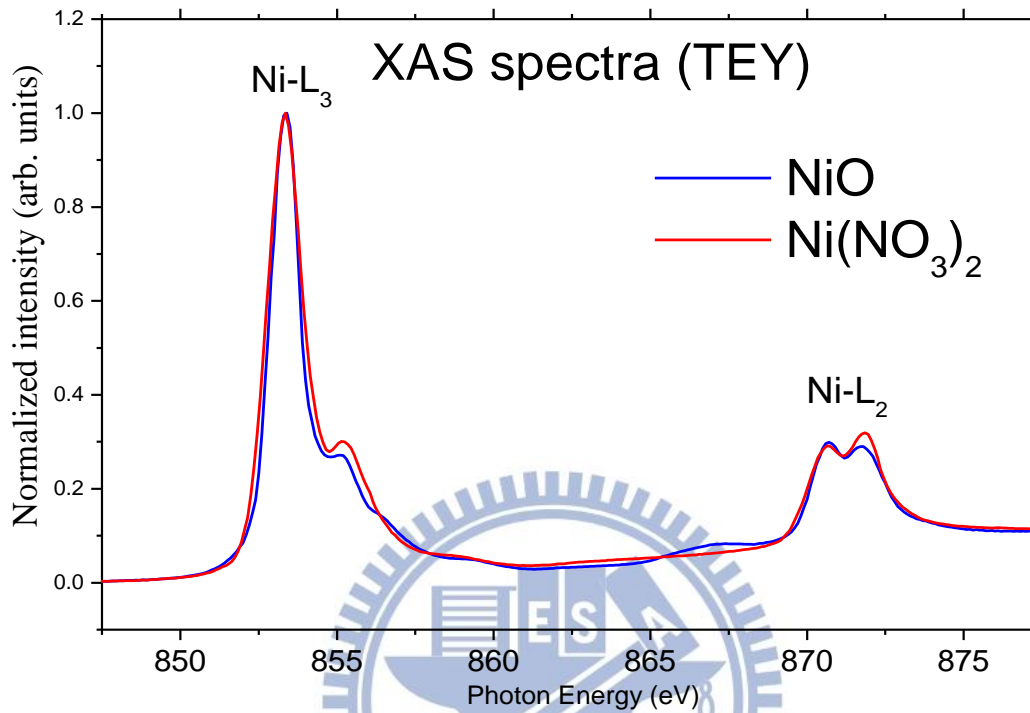


Fig. 4-3. Nickel  $L_{2,3}$  edge XAS data in TEY.

Since two nickel sites in Ni(NO<sub>3</sub>)<sub>2</sub> have different distorted NiO<sub>6</sub> octahedral local environment, and the distortion may cause the presence of low spin state, first, we suspect whether all divalence nickel stay in pure low spin state in Ni(NO<sub>3</sub>)<sub>2</sub>. The Ni<sup>2+</sup> low spin state has six electrons in the  $t_{2g}$  state and two electrons stay in one orbital of  $e_g$  state, this cause the LS spectrum has only one single peak in both  $L_{2,3}$  edge[11]. Compare with the calculated XAS spectra of Ni<sup>2+</sup> LS in Fig.4-5, the line shape and the intensity ratio in  $L_3$ -edge of Ni(NO<sub>3</sub>)<sub>2</sub> tells that it is not a pure low spin spectra[10,11]. Second, we think about an inhomogeneous mixed spin state in the Ni(NO<sub>3</sub>)<sub>2</sub>, which means the higher intensity at 855.1 eV and 871.8 eV may be the



contribution from some LS population. Fig. 4-6 shows the  $\text{Ni}^{2+}$  HS-LS mixed spectra from Dr. S.M. Peng et al who studied one-dimensional nickel material [12]. The bottom spectrum shows a  $\text{Ni}^{2+}$  2HS+7LS spectrum, the mean peak in  $L_3$ -edge come from the LS contributions, the energy position is 1 eV higher than the mean peak of  $\text{Ni}^{2+}$  HS spectra (top one) and sits between the mean peak and the second peak of HS spectrum. Comparing with the energy position, we assume the higher intensity at 855.1 eV and 871.8 eV are not the contribution from LS spectra. At the end, we assume all divalence nichels stay in high spin state in  $\text{Ni}(\text{NO}_3)_2$ , and the spectra shape difference between  $\text{NiO}$  and  $\text{Ni}(\text{NO}_3)_2$  may come from those different local environments, which means an undistorted  $\text{NiO}_6$  octahedral cluster in  $\text{NiO}$  and two closely distorted  $\text{NiO}_6$  octahedral in  $\text{Ni}(\text{NO}_3)_2$  ( see Fig. 2-4).

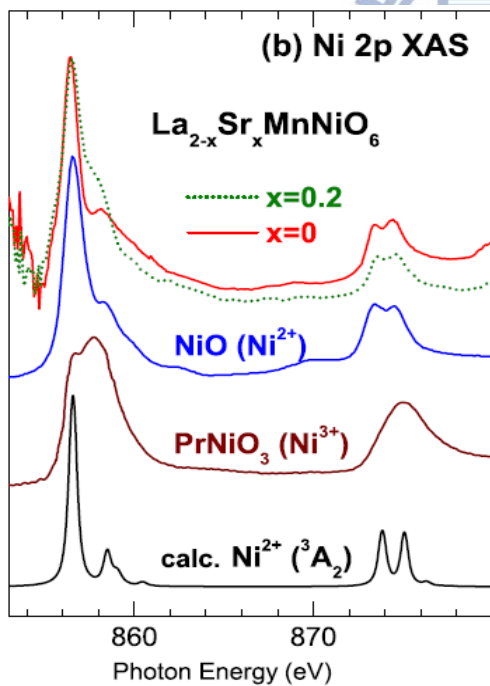


Fig. 4-4. Ni 2p XAS spectra[10]

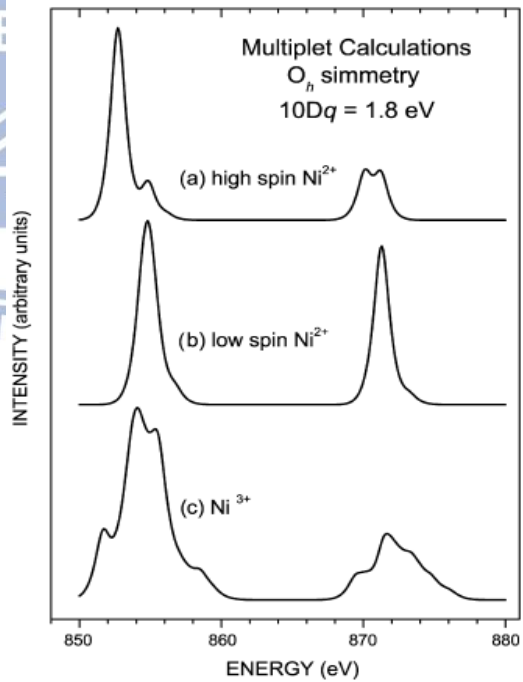


Fig. 4-5 Ni<sup>2+</sup> XAS simulation from [11]

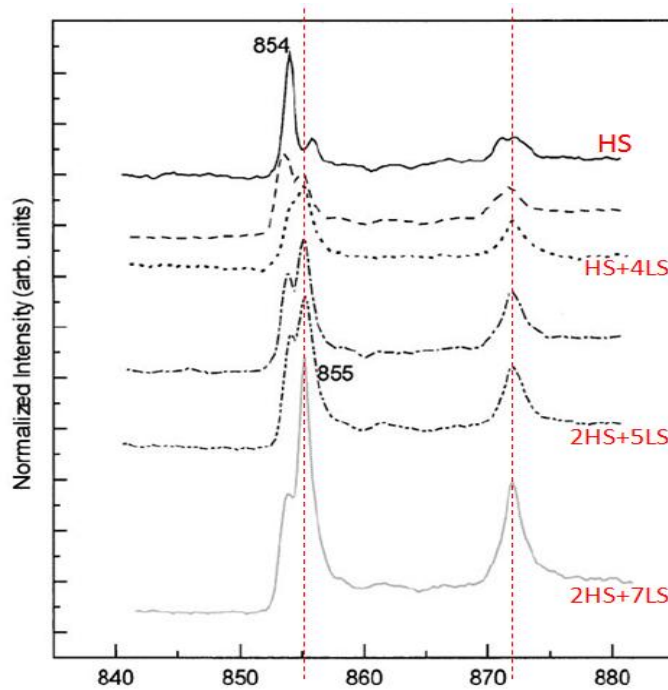


Fig. 4-6 Ni<sup>2+</sup> HS-LS mixed XAS spectra[12]

### 4-3 XANES theoretical calculation by XTLS

To confirm the spin state of divalent nickel in Ni(NO<sub>3</sub>)<sub>2</sub>, we also discussed the theoretical calculations of  $L_{2,3}$  XAS line shape using the full atomic multiplet theory, together with hybridization of Ni 3d orbital with the O 2p ligands and the point charge crystal field in NiO<sub>6</sub> cluster [8].

For NiO case, the NiO<sub>6</sub> octahedral is almost undistorted and nickel ion has same distance between all six O neighbors. In our calculations, we use the hybridization coefficient  $pd\sigma = -1.29$  eV [13], set  $\Delta e_g = 0$  eV (undistorted octahedral). We focus on the peak splitting and ratio of intensity in both  $L_2$  and  $L_3$  edge, a shoulder at 856.5 eV and a charge transfer characteristic at 859 eV. Finally we get a best fit to NiO spectra in  $10Dq=1.0$  eV.

For Ni(NO<sub>3</sub>)<sub>2</sub> case, the crystal structure shows the average Ni–O bond length is 2.071 Å, this value is very close to the bond length of 2.08(1) Å in NiO [14,15]. Since

NiO and Ni(NO<sub>3</sub>)<sub>2</sub> have a closely average Ni—O bond length, their 10Dq should also be closed. We focus on the peak splitting and intensity ratio in both L<sub>2</sub> and L<sub>3</sub> edge, our calculations shows 10Dq=1.0 eV, Δe<sub>g</sub>=0.8 eV and 10Dq=0.9 eV, Δe<sub>g</sub>=0.7 eV can fit the Ni(NO<sub>3</sub>)<sub>2</sub> spectra, and 10Dq=0.9 eV, Δe<sub>g</sub>=0.7 eV is the best fit to Ni(NO<sub>3</sub>)<sub>2</sub> spectra while the L<sub>3</sub> edge looks too broad in Δe<sub>g</sub>=0.8 eV calculation. Fig. 4-7 shows the best fitting on Ni(NO<sub>3</sub>)<sub>2</sub>, Δe<sub>g</sub>=0.7 eV comes from the distorted NiO<sub>6</sub> cluster.

The calculation result of 10Dq=0.9 eV, Δe<sub>g</sub>=0.7 eV shows triply degenerate ground state with total spin S(S+1)=1.9988(1), and S(S+1)=1.9746 in the first excited state. The energy of first excited state is 0.98 eV higher than the triply degenerate ground state, the energy difference is too high for the thermal excitation at room temperature.

In our calculations we consider the point charge crystal field and hybridization with ligands separately, we called as ligand field model(LFM). Given the fact that various X-ray absorption studies use 10Dq around 1.6~1.8 eV to fit NiO spectra [11,16,17], that's because the octahedral crystal and ligand field splitting are included in one single effective parameter 10Dq, we called as a free ion model(FIM) approach. 10Dq is the t<sub>2g</sub>/e<sub>g</sub> orbital splitting in octahedral symmetry. We also tried the FIM calculations (pdσ = 0 eV), and shows 10Dq=1.6 eV, Δe<sub>g</sub>=0 eV can fit NiO spectra well, while 10Dq=1.5 eV, Δe<sub>g</sub>=0.6 eV result can fit Ni(NO<sub>3</sub>)<sub>2</sub> well(see Fig.4-8). The 10Dq=1.5, Δe<sub>g</sub>=0.6 eV calculation shows S(S+1)=1.9984(2), also a HS state. Either LFM or FIM calculations represent the nickel ions is divalence and still with a high spin state S=1 in Ni(NO<sub>3</sub>)<sub>2</sub>, like those nickel ions in NiO. Compare the FIM and LFM calculations, the LFM can get more splitting and fit beter in L<sub>2</sub> edge. The different spectra shape come from their different ligand field multiplet effect, which means an undistorted NiO<sub>6</sub> octahedral in NiO and two closely distorted octahedral in Ni(NO<sub>3</sub>)<sub>2</sub>.

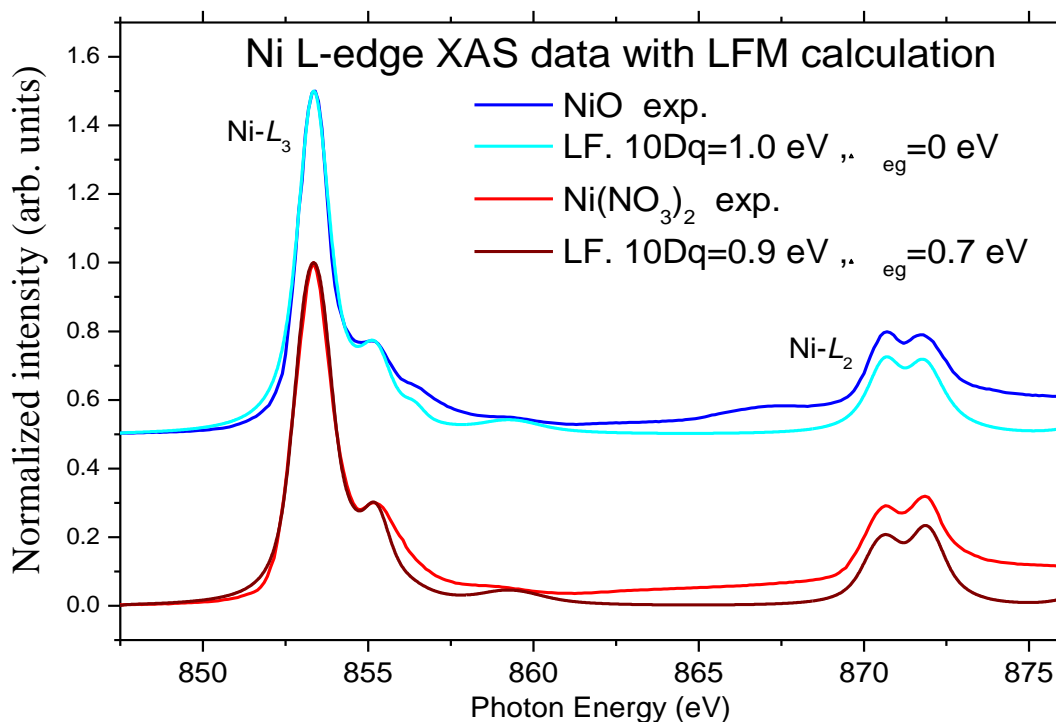


Fig. 4-7. Nickel  $L_{2,3}$  edge XAS data with ligand field model calculations.

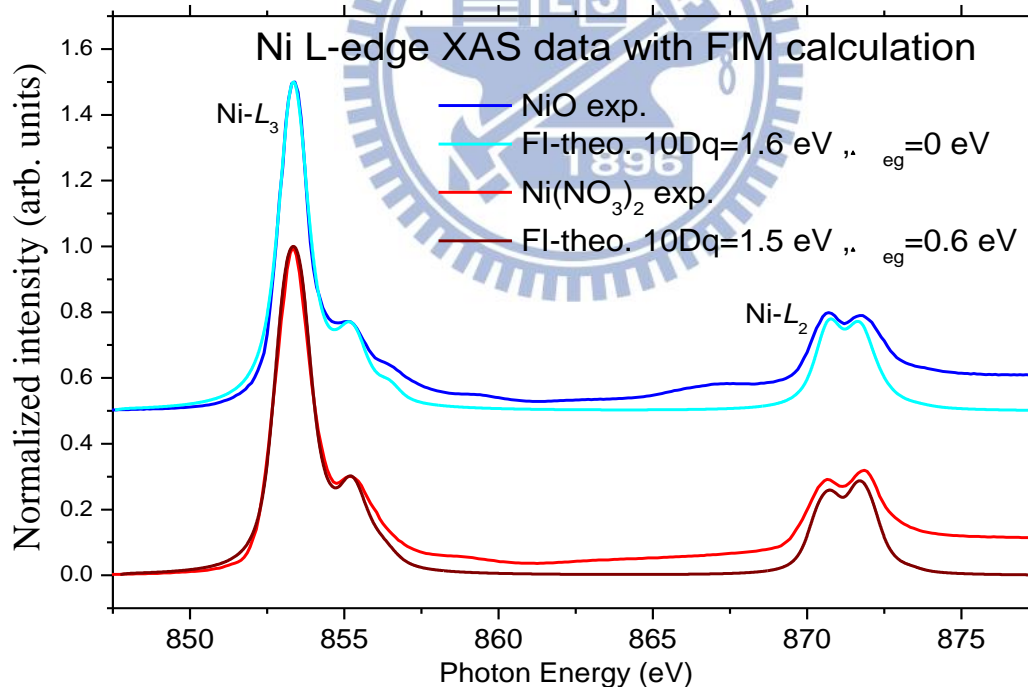


Fig. 4-8. Nickel  $L_{2,3}$  edge XAS data with free ion model calculations.

#### 4-4 Conclusions of Ni(NO<sub>3</sub>)<sub>2</sub>

First, the XAS spectra shows the divalence nickel in Ni(NO<sub>3</sub>)<sub>2</sub> compound. Combine with the theoretical calculation, we assume that the divalence nickel shows a high spin state  $S=1$  in Ni(NO<sub>3</sub>)<sub>2</sub>, same as NiO. The spectrum shape differences between NiO and Ni(NO<sub>3</sub>)<sub>2</sub> come from the different local environments.

On the other hand, very recently, O. Volkova et al. [2] measured magnetization measurement under magnetic field as shown in Fig. 4-9, the obtained value of saturation moment amounts about 2.03  $\mu_B$ /f.u. which is very close to the theoretical one  $M_S = ngS\mu_B = 2.15 \mu_B$ /f.u. for Ni<sup>2+</sup>,  $S=1$ , which is consistent to our simulations.

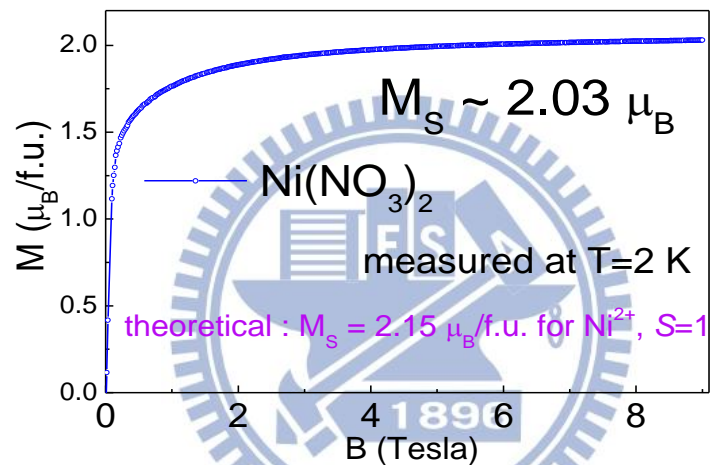


Fig. 4-9. Magnetization measurement of Ni(NO<sub>3</sub>)<sub>2</sub> At 2 K under magnetic field.[2]

## Chapter 5. Results and discussion on PrSrCoMnO<sub>6</sub>

To study the valence and spin state of transition metal ions in polycrystal PrSrCoMnO<sub>6</sub> sample, and expect to see the existence of Co<sup>3+</sup> high spin state in perovskite structure, we measured the X-ray absorption near edge spectroscopy (XANES) on Co K-edge, Co L-edge, Mn K-edge and Mn L-edge in polycrystal PrSrCoMnO<sub>6</sub> sample.

### 5-1 Experimental Design

In one paper studied on LaSrCoMnO<sub>6</sub> sample from J. Androulakis[3]. They assume the valence is +4 for manganese ion, and +3 for cobalt ions, and the trivalence cobalt may stay in intermediate-spin state (3d<sup>6</sup>, S=1) or high-spin state (3d<sup>6</sup>, S=2). Since PrSrCoMnO<sub>6</sub> and LaSrCoMnO<sub>6</sub> belong to the same series, we wonder whether the valence and spin state of transition metal changed in different rare earth compound. The Co K-edge and Mn K-edge XAS experiments were performed at the BL17C at the National Synchrotron Radiation Research Center (NSRRC) in Taiwan. The Co L-edge and Mn L-edge XAS experiments were performed at both H-SGM beam line and Dragon beam line in NSRRC Taiwan. We also combine with the X-ray diffraction refinement and theoretical calculations to investigate the relationship between XAS spectra with crystal structure.

### 5-2 Mn XANES spectra

Room temperature Mn L-edge XAS data was recorded in total electron yield (TEY) mode (see Fig.5-1). In the previous work, which shows the PrSrCoMnO<sub>6</sub> sample has a similar spectra shape and energy position with MnO<sub>2</sub>, we infer that the valence on manganese ion should be Mn<sup>4+</sup>.

Room temperature Mn *K*-edge XAS was recorded in the transmission mode. The edge position is sensitive to Mn valence in the *K*-edge spectra, which also represents the Mn<sup>4+</sup> in PrSrCoMnO<sub>6</sub> sample (see Fig.5-2), same as those Mn<sup>4+</sup> in Eu<sub>2</sub>CoMnO<sub>6</sub> and La<sub>2</sub>CoMnO<sub>6</sub> double perovskite[18,19,20].

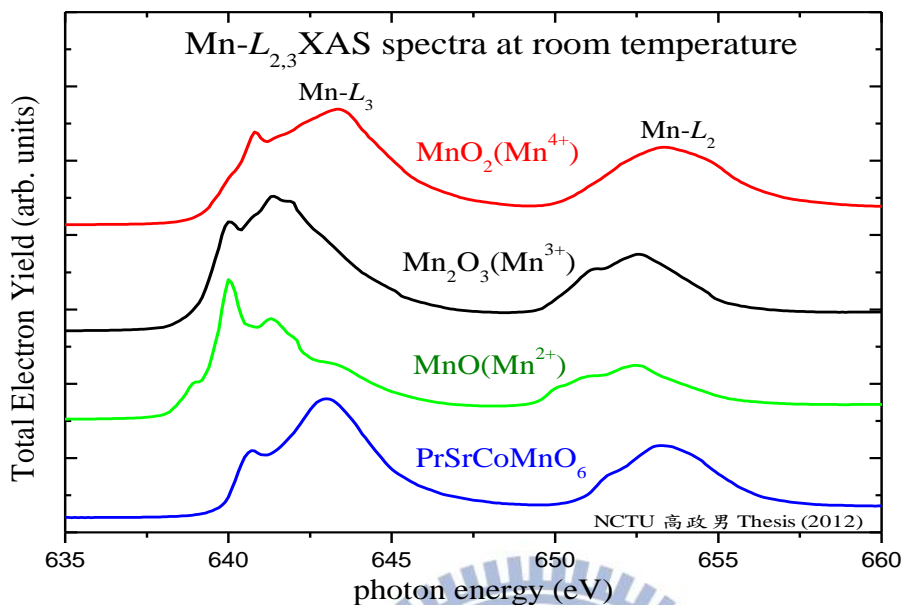


Fig. 5-1 Mn *L*-edge XAS data in TEY mode

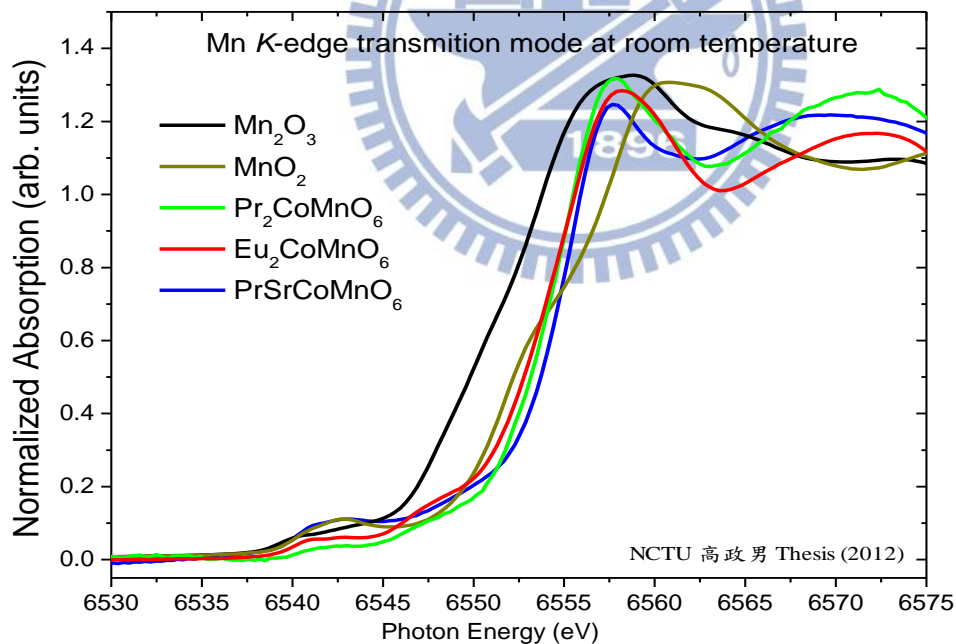


Fig. 5-2 Mn *K*-edge XAS data in transmission mode

### 5-3 Co XANES spectra

In Co *K*-edge, room temperature XAS was recorded in the transmission mode from BL.17C in NSRRC Taiwan, as shown in Fig.5-3. The *K*-edge XAS spectra is very sensitive to the valence of transition metal ions. Compare with other reference spectra, we find the PrSrCoMnO<sub>6</sub> spectrum is very similar to EuCoO<sub>3</sub>, and we infer that the cobalt ions are also trivalence in PrSrCoMnO<sub>6</sub> sample.

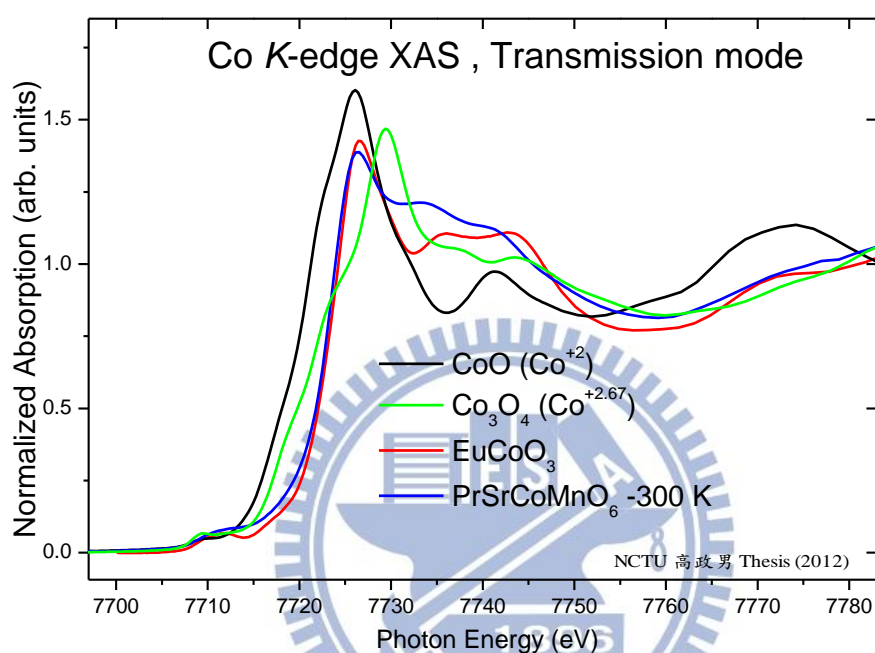


Fig.5-3. Co *K*-edge XAS spectra in transmission mode

In Co *L*-edge, room temperature XAS experiments were performed at the H-SGM beamline in NSRRC. Clean sample surface were obtained by cleaving samples in chamber with pressure lower than 10<sup>-7</sup> mbar. XAS data was recorded in total electron yield (TEY) in ultra high vacuum (~10<sup>-10</sup> mbar) chamber.

To estimate the valence and spin state of cobalt ions in PrSrCoMnO<sub>6</sub> sample, we compare the XAS data with some reference sample in Fig.5-4, such as CoO(Co<sup>2+</sup>), EuCoO<sub>3</sub>(Co<sup>3+</sup>-LS) and Sr<sub>2</sub>CoO<sub>3</sub>Cl<sub>2</sub>. If we compare with the divalence cobalt standard sample CoO, we find that the spectrum shape of PrSrCoMnO<sub>6</sub> is far away from CoO,



and PrSrCoMnO<sub>6</sub> sits in a higher energy position, means the cobalt ions are not pure divalence. To think about the Co<sup>2+</sup>-Co<sup>3+</sup> mixed valence state, C. F. Chang[21] mentioned about the spectra shape of Co<sup>2+</sup>-Co<sup>3+</sup> mixed valence state looks like Co<sup>3+</sup> high spin state (see Fig. 5-5), but we still can distinguish them from the L<sub>3</sub>-edge mean peak energy position and a Co<sup>2+</sup> characteristic at 777.7eV. Fig. 5-6 shows the Co<sup>3+</sup>-Co<sup>4+</sup> mixed valence state studied by H.-J. Lin [22] . In Co<sup>4+</sup> XAS spectra, the mean peak in L<sub>3</sub>-edge is 1.5 eV higher than the mean peak of Co<sup>3+</sup> spectra, and Co<sup>4+</sup> spectra also present an obvious peak at 779.4 eV. Both the characteristics of Co<sup>4+</sup> spectra were not displayed in PrSrCoMnO<sub>6</sub> spectrum. So far, we assume the cobalt ions are trivalence in PrSrCoMnO<sub>6</sub> sample, consistent with the Co K-edge.

In the Co L-edge XANES spectra, PrSrCoMnO<sub>6</sub> shows a very different look with those ReCoO<sub>3</sub> perovskite (Re=Eu, Sm). According to Z. Hu et al.(2004)[4], they mentioned about the cobalt ions shows trivalence in EuCoO<sub>3</sub> single crystal sample. The Co<sup>3+</sup> ions formed an octahedral coordination with the six oxygen neighbours and Co<sup>3+</sup> stays in the low spin state (LS, 3d<sup>6</sup>, S=0). In the Co<sup>3+</sup> LS XAS spectrum, there shows a mean peak and a shoulder characteristic at higher energy range in both L<sub>2</sub> and L<sub>3</sub>-edge. Contrarily, Co L-edge XANES spectrum of PrSrCoMnO<sub>6</sub> is slightly similar to the spectrum of layered Sr<sub>2</sub>CoO<sub>3</sub>Cl compound, which was studied by Z. Hu et al.(2004)[4]. Z. Hu et al. demonstrate that the Co<sup>3+</sup> ions with the CoO<sub>5</sub> pyramidal coordination in the layered Sr<sub>2</sub>CoO<sub>3</sub>Cl compound shows an unambiguously high spin state (HS, 3d<sup>6</sup>, S=2). In the HS spectrum, there shows a mean peak and a shoulder characteristic in the lower energy range in L<sub>3</sub>-edge, while there are two shoulders in the L<sub>2</sub>-edge, one stays in the higher energy range than mean peak and another one stays in the lower energy range.

If we compare the PrSrCoMnO<sub>6</sub> XAS spectrum with other trivalence cobalt spectra more carefully, we can find that the L<sub>3</sub>-edge of PrSrCoMnO<sub>6</sub> spectrum is very

similar to  $\text{Sr}_2\text{CoO}_3\text{Cl}_2$   $\text{Co}^{3+}$  HS state, but the  $L_2$ -edge looks like the combination of  $\text{Co}^{3+}$  HS and LS spectra. We are interested in such an unusual phenomenon.

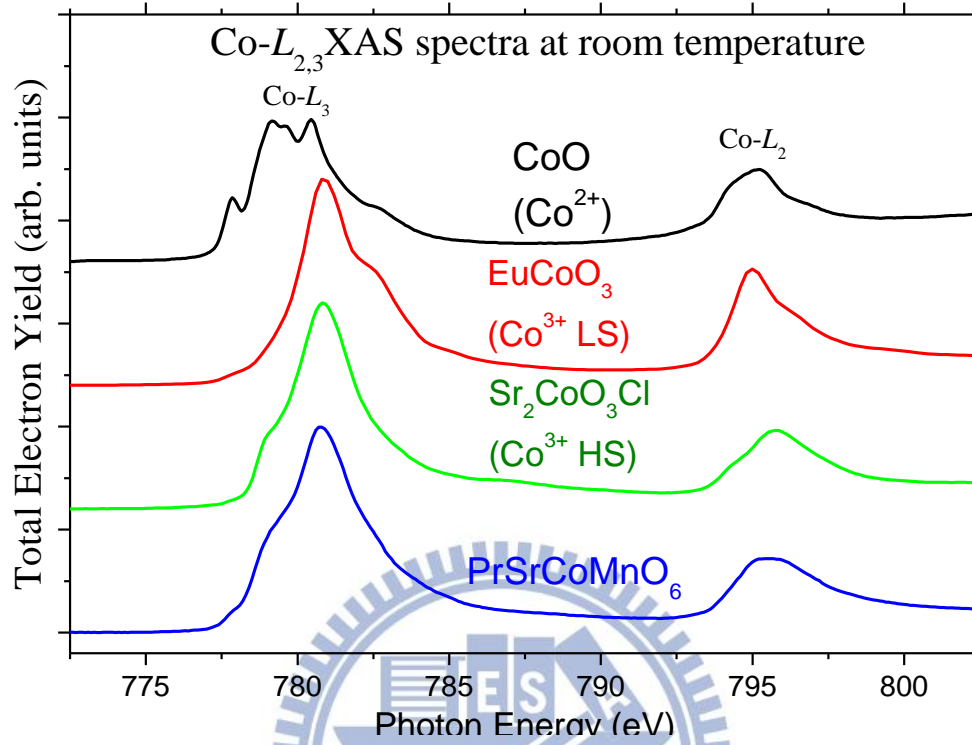


Fig. 5-4 Co  $L$ -edge XAS data

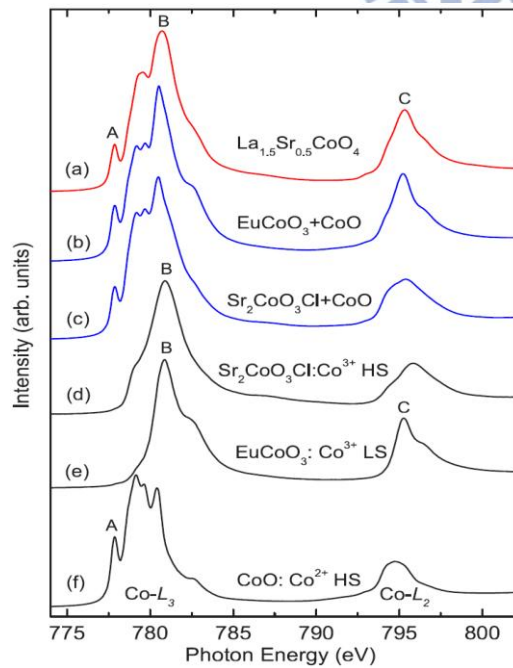


Fig. 5-5 Co  $L$ -edge spectra from ref.[21]

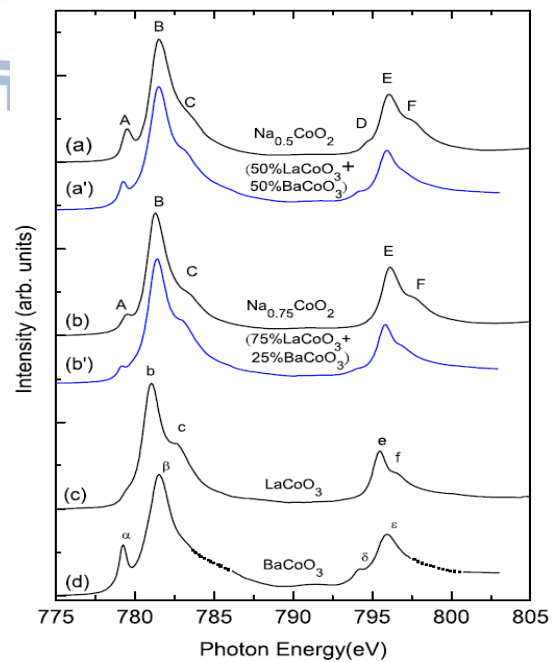


Fig. 5-6 Co  $L$ -edge spectra [22]

In order to study the spin state of  $\text{Co}^{3+}$  ions in  $\text{PrSrCoMnO}_6$ , we also measured the temperature dependent Co  $L$ -edge XAS spectra at Dragon beam line in NSRRC. The temperature dependent Co  $L$ -edge spectra is shown in Fig. 5-7, we find a shoulder characteristic presence at lower energy range of  $L_3$ -edge in all temperature, and the shoulder intensity decrease with temperature decreasing. On the other hand, the intensity of peak at 795eV in  $L_2$ -edge increase with temperature decreasing.

We focus on the  $L_3$ -edge first, there shows a shoulder characteristic in the lower energy range, which is the contribution from  $\text{Co}^{3+}$  HS state. As the temperature increasing, the shoulder intensity also increases. We infer that the HS population increases with temperature increasing. Now turn to the  $L_2$ -edge, there shows a peak at 795eV which come from  $\text{Co}^{3+}$  LS spectra. As the temperature increasing, we saw the peak intensity become lower. We infer that the LS population decreases with the temperature increasing, this result consists with that in the  $L_3$ -edge. Up to now, we assume that the  $\text{Co}^{3+}$  ions in  $\text{PrSrCoMnO}_6$  sample is an HS-LS mixed-spin state system, and the HS state presence more at higher temperature.

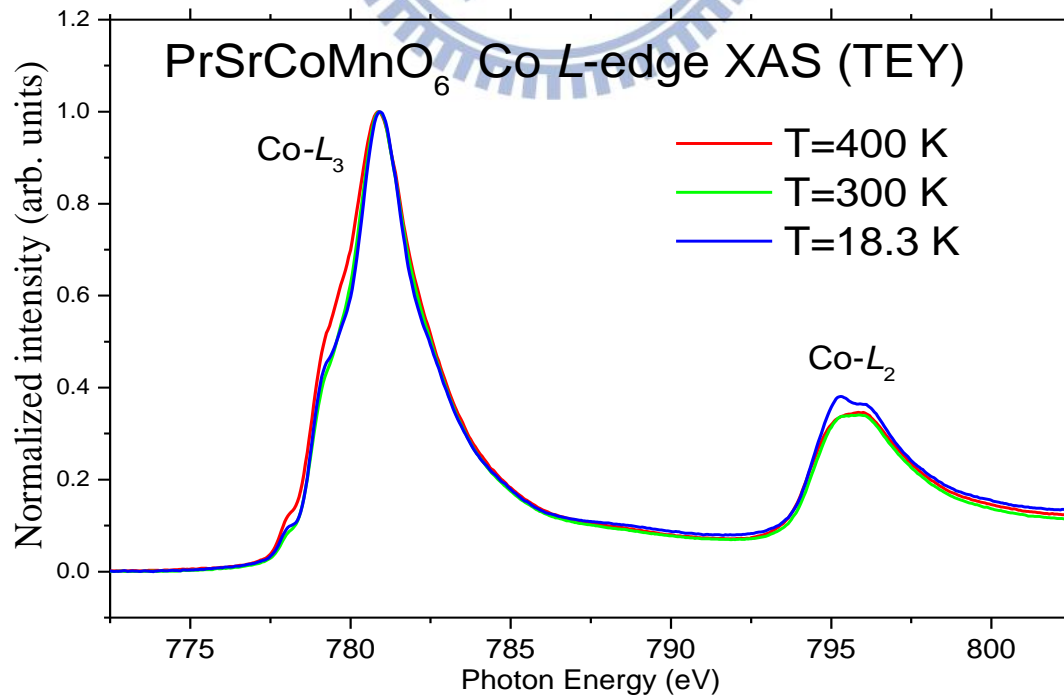


Fig. 5-7 Temperature dependent Co  $L$ -edge XAS spectra on  $\text{PrSrCoMnO}_6$  sample

## 5-4 Powder X-ray diffraction

The X-ray diffraction experiment of powder PrSrCoMnO<sub>6</sub> sample is done by the Bruker D8 diffractometer with Cu K $\alpha$  radiation. The Rietveld refinement is done by the Bruker DIFFRAC.TOPAS software. Fig.5-8,9(a~d) shows the room-temperature XRD results of PrSrCoMnO<sub>6</sub>, blue curve represents the experiment data, red curve represents the simulation result from Rietveld refinement, and the green curve represents the difference between experiment data with simulation. The crystal structure is solved to have monoclinic  $P21_n$  space group [ $a=5.401453(53)$  Å,  $b=5.427901(50)$  Å,  $c=7.663798(70)$  Å;  $\alpha=\gamma=90.0$  degree and  $\beta=89.55283(63)$  degree] as shown in the Fig.5-10.

For room-temperature XRD data, Rietveld refinement gives two sites for transition metals in table 5-1, both sites have six oxygen around and form a TMO<sub>6</sub> octahedral coordination. Since the XRD can only tell the distance around but not atoms, we tried to distinguish them from some reference. First we compare the average Mn-O bond length between PrSrCoMnO<sub>6</sub> to La<sub>1-x</sub>Ca<sub>x</sub>MnO<sub>3</sub> perovskite,  $x=0, 0.3, 0.5, 0.9$  and  $x=1$  in table 5-2[23~27]. For a higher valence of Mn ion, the average bond length should become shorter, so the site-2 has more chance to be the Mn site. Second, we compare with the La<sub>2-x</sub>Sr<sub>x</sub>CoMnO<sub>6</sub> ( $x=0$  and  $0.4$ ) double perovskite[28,29] in table 5-3, which also show site-2  $\langle\text{Mn-O}\rangle=1.9202$  Å might be the Mn site. Now we compare the average Co-O bond length of CoO<sub>6</sub> coordination with ReCoO<sub>3</sub> (Re=Eu, Sm, La) perovskite[30~32] in table 5-4, which are all Co<sup>3+</sup> case.

In the CoO<sub>6</sub> octahedral environment, the Co 3d degenerate state was separated into  $e_g$  and  $t_{2g}$  state with  $10Dq$  difference by the crystal field, and the  $e_g$  state was separated into  $x^2-y^2$  and  $3z^2-r^2$  with  $\Delta e_g$  difference by the distortion. Depending on the ratio between Hund's coupling  $10Dq$  and  $J_H$  splitting, Co<sup>3+</sup> ions ( $3d^6$ ) may exhibit either low-spin (LS,  $S=0$ ) or high-spin (HS,  $S=1$ ) states as shown in Fig.5-11.

An easy way to calculate the total energy of HS or LS state is to set the  $t_{2g}$  energy level to be zero, gain one crystal field energy  $10Dq$  for each electron which stays in the  $e_g$  state, and also consider about the exchange interaction (Hund's coupling) between each  $3d$  electrons.

$$E_{total} = E_{C.F} + E_{ex}$$

$$E_{ex} = -\left[\frac{n(n-1)}{2} + \frac{m(m-1)}{2}\right]J_H$$

$n$  is the number of spin up electrons,  $m$  is the number of spin down electrons,  $J_H$  is the Hund's coupling energy. For  $Ni^{2+}$ , the total energy of HS and LS can be describe as :

$$E_{HS} = 2 * 10Dq - 10J_H$$

$$E_{LS} = 0 * 10Dq - 6J_H$$

$$E_{HS} - E_{LS} = 10Dq - 4J_H$$

HS state would be ground state in a small crystal field case.

In the Co L-edge XAS data,  $PrSrCoMnO_6$  shows a high spin like spectrum shape and  $ReCoO_3$  shows low spin spectra, which means the crystal field in  $PrSrCoMnO_6$  is smaller than those three else, so Co ions should stay in site-1 and have the longest average Co-O bond length 1.9342 Å .

To give a summary, at room temperature, Co ion has a average Co-O bond length of 1.937 Å in the  $CoO_6$  coordination, and Mn ion has a average Mn-O bond length of 1.920 Å in the  $MnO_6$  coordination.

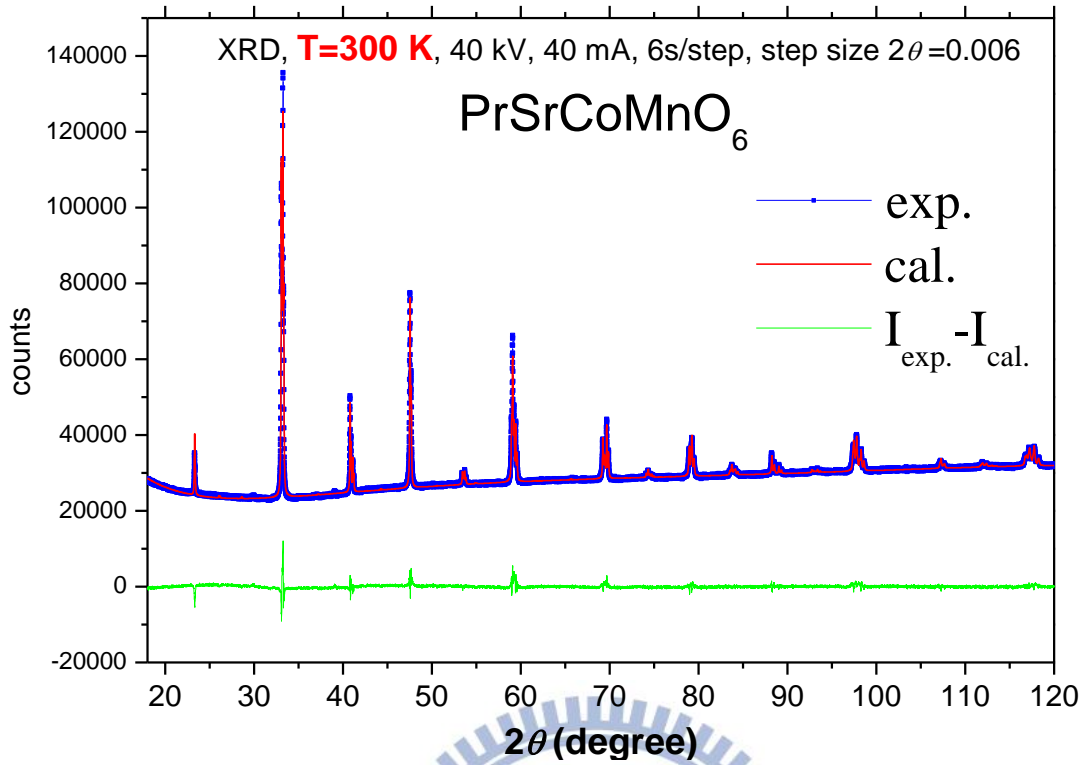


Fig.5-8 X-ray diffraction data of powder PrSrCoMnO<sub>6</sub> sample

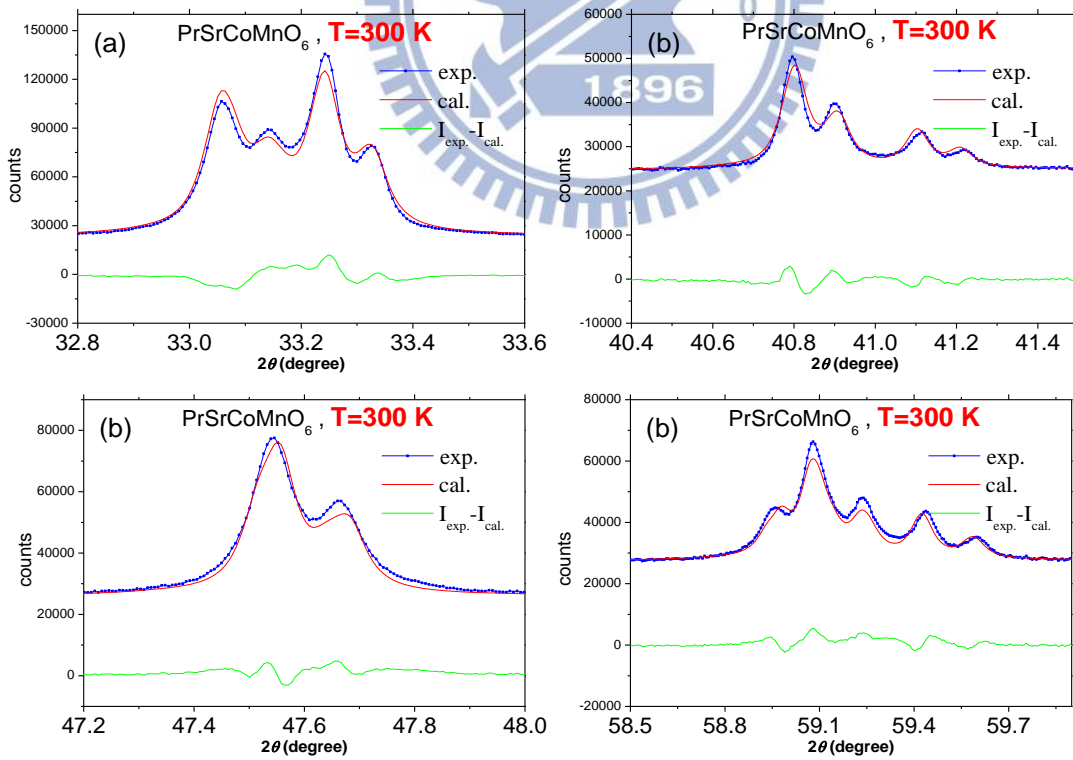


Fig.5-9(a,b,c,d) Details of X-ray diffraction data and simulations on PrSrCoMnO<sub>6</sub>.

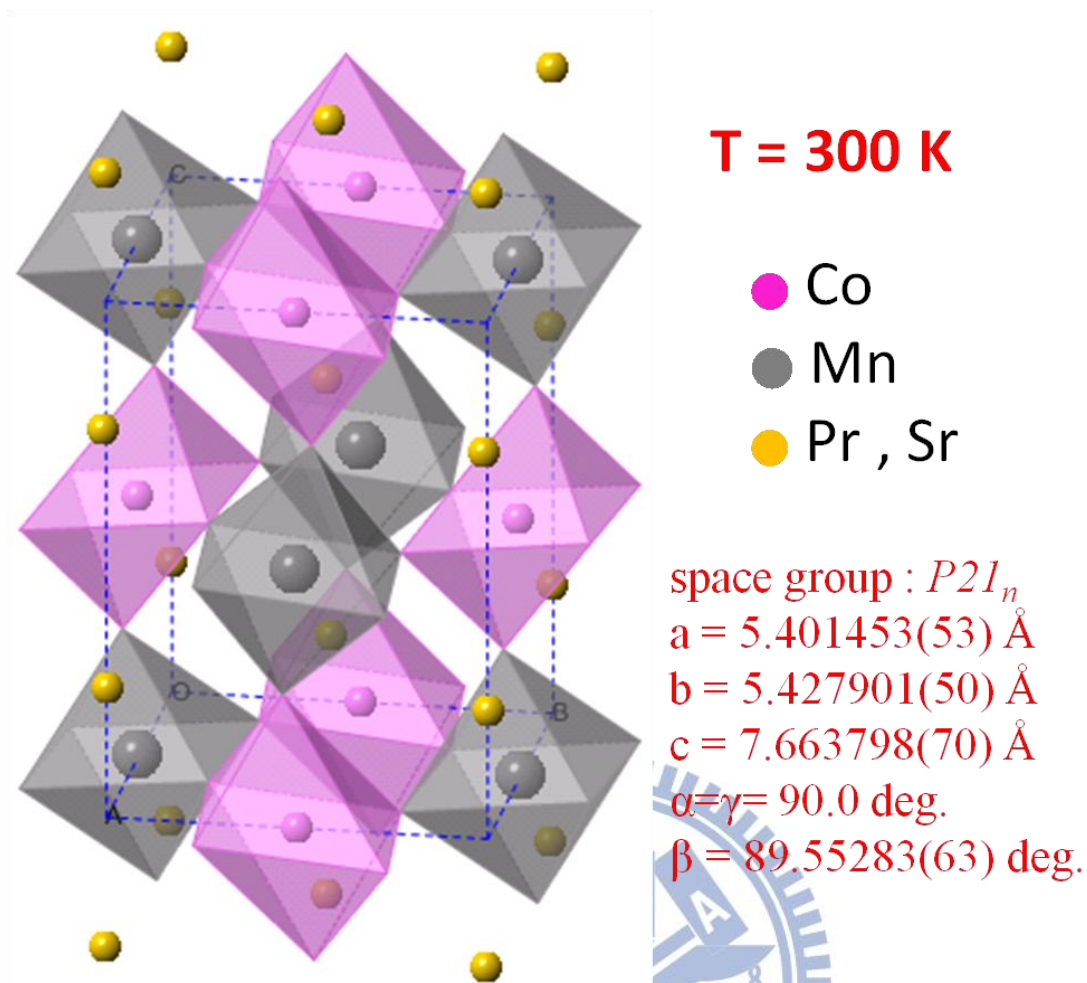


Fig.5-10 Solved crystal structure of PrSrCoMnO<sub>6</sub> at T=300 K.

	Site-1	Site-2
Co/Mn-O <sub>1</sub> (Å)	1.87(11)	1.98(12)
Co/Mn-O <sub>2</sub> (Å)	1.97(12)	1.89(12)
Co/Mn-O <sub>3</sub> (Å)	1.970(73)	1.889(73)
$d_{\text{ave}}$ (Å)	1.937(101)	1.920(104)

Table 5-1. TM-O bond length of two TM sites

	Mn <sup>4+</sup>		Mn <sup>4+</sup>	Mn <sup>3.9+</sup>	Mn <sup>3.5+</sup>	Mn <sup>3.3+</sup>	Mn <sup>3+</sup>
	PrSrCoMnO <sub>6</sub> Site 1	PrSrCoMnO <sub>6</sub> Site 2	CaMnO <sub>3</sub>	La <sub>0.1</sub> Ca <sub>0.9</sub> MnO <sub>3</sub>	La <sub>0.5</sub> Ca <sub>0.5</sub> MnO <sub>3</sub>	La <sub>0.7</sub> Ca <sub>0.3</sub> MnO <sub>3</sub>	LaMnO <sub>3</sub>
Mn-O <sub>1</sub>	1.870	1.980	1.888	1.913	2.042	1.999	<1> 1.948 <2> 1.973 <3> 1.954
Mn-O <sub>2</sub>	1.970	1.890	1.887	1.914	1.923	2.075	<1> 2.012 <2> 1.973 <3> 1.904
Mn-O <sub>3</sub>	1.970	1.889	1.906	1.890	1.927	1.886	<1> 1.945 <2> 1.973 <3> 2.131
d <sub>ave</sub>	1.937	<b>1.920</b>	1.8937	1.9057	1.964	1.9867	<1> 1.9683 <1> 1.9730 <1> 1.9963

Table 5-2. Mn-O bond length in MnO<sub>6</sub> coordination

sample	PrSrCoMnO <sub>6</sub>	La <sub>1.6</sub> Sr <sub>0.4</sub> CoMnO <sub>6</sub>	La <sub>2</sub> CoMnO <sub>6</sub>
valence of Co	Co <sup>3+</sup>	Co <sup>2.4+</sup>	Co <sup>2+</sup>
<Co-O> (Å)	1.937	1.9657	2.03867
valence of Mn	Mn <sup>4+</sup>	Mn <sup>4+</sup>	Mn <sup>4+</sup>
<Mn-O> (Å)	1.920	1.9206	1.9173
reference	me	J. Exp. Theor. Phys 99, 2, (2004), 363–369 I. O. Troyanchuk et. al	Eur. Phy. J.B. 84, 357-364(2011) X. Lan et. al

Table 5-3. Mn-O bond length in double perovskite samples

	PrSrCoMnO <sub>6</sub> Site 1	PrSrCoMnO <sub>6</sub> Site 2	EuCoO <sub>3</sub>	SmCoO <sub>3</sub>	LaCoO <sub>3</sub>
Co-O <sub>1</sub>	1.870	1.980	1.926(9)	1.919	1.932(1)
Co-O <sub>2</sub>	1.970	1.890	1.942(9)	1.934	1.932(1)
Co-O <sub>3</sub>	1.970	1.889	1.921(3)	1.926	1.932(1)
d <sub>ave</sub>	<b>1.937</b>	1.920	1.9297	1.9263	1.932(1)
	<b>HS</b>		<b>LS</b>	<b>LS</b>	<b>LS</b>

Table 5-4. Co-O bond length in CoO<sub>6</sub> coordination



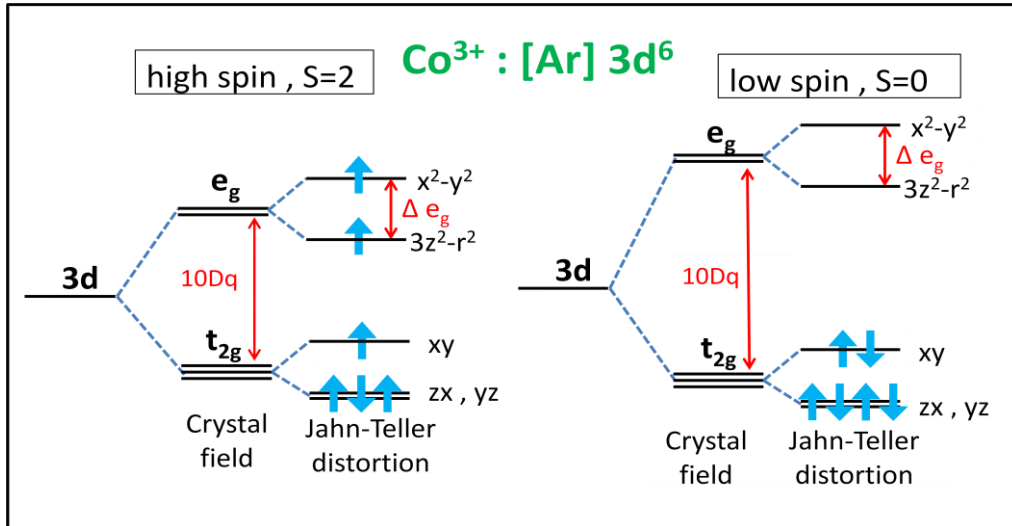


Fig. 5-11. High spin and low spin in Ni<sup>2+</sup> (3d<sup>8</sup>) case.

On the other hand, we also did the XRD experiment on PrSrCoMnO<sub>6</sub> at T=12 K. The XRD data and the Rietveld refinement results are shown in the Fig.5-12,13(a~d). The low temperature crystal structure is solved to have monoclinic  $P21_n$  space group [a=5.438825(83) Å, b=5.395555(91) Å, c=7.62190(12) Å;  $\alpha=\gamma=90.0$  degree and  $\beta=89.9572(19)$  degree] as shown in Fig.5-14. The solved crystal structure also shows two transition metal sites with different TM-O bond length. Table 5-5 shows the comparison of lattice parameter in PrSrCoMnO<sub>6</sub> between T=300 K and T=12 K. PrSrCoMnO<sub>6</sub> still keeps the space group  $P21_n$  at low temperature, same as that in the room temperature. An interesting thing is that the lattice volume become smaller and the average Mn-O bond length also become shorter at low temperature, but the average Co-O bond length become 1.980(57) Å at low temperature, which is longer than the Co-O bond length at room temperature.

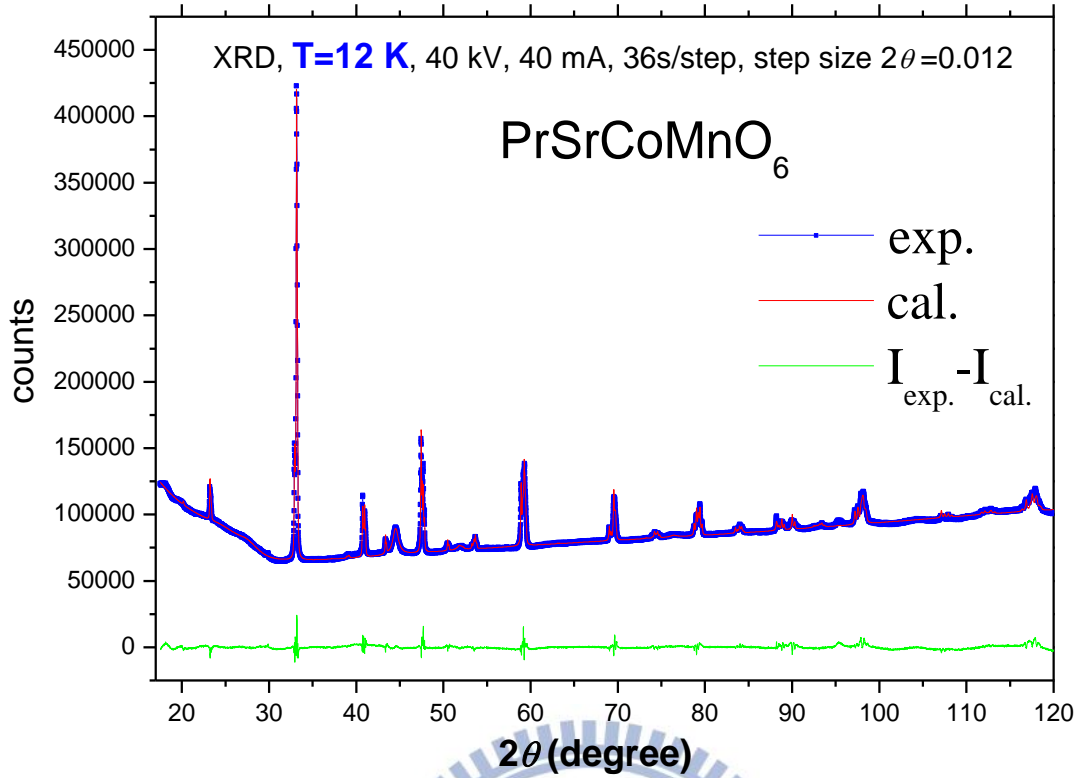


Fig.5-12 X-ray diffraction data of powder  $\text{PrSrCoMnO}_6$  sample at  $T=12$  K.

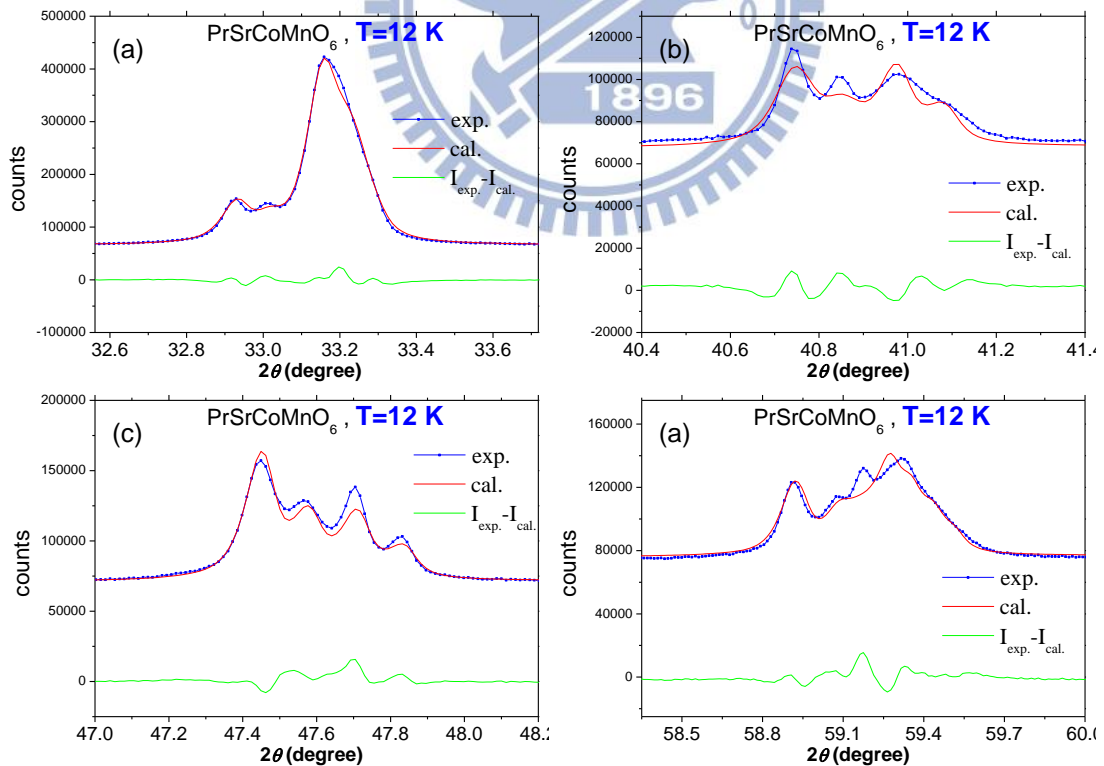


Fig.5-13 (a,b,c,d) Details of X-ray diffraction data and simulations on  $\text{PrSrCoMnO}_6$  at  $T=12$  K

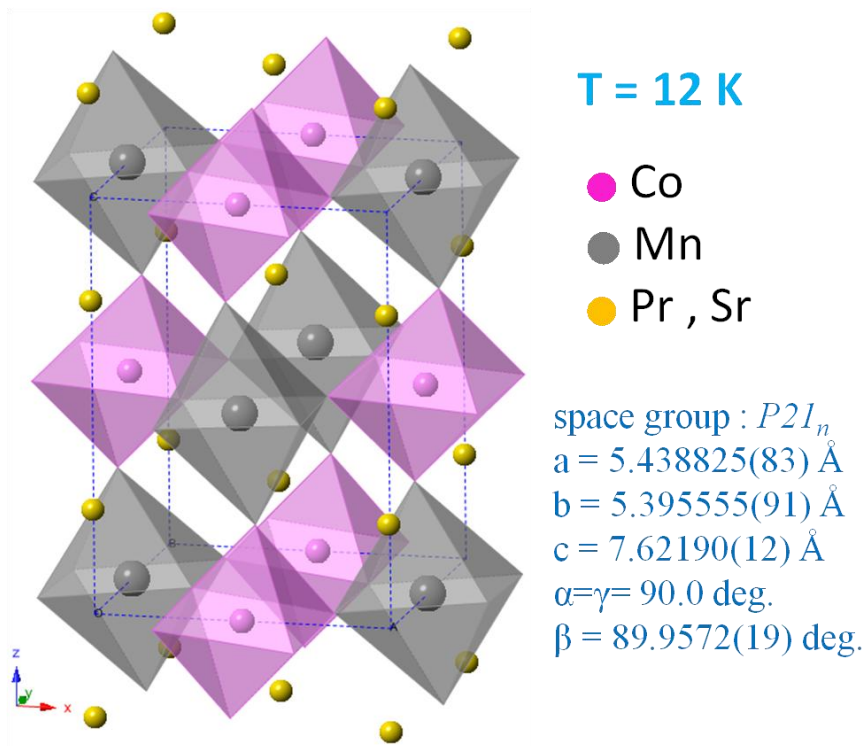


Fig.5-14 Solved crystal structure of PrSrCoMnO<sub>6</sub> at T=12 K.

	<b>T = 300 K</b>		<b>T = 12 K</b>	
space group	$P21/n$		$P21/n$	
a (Å)	5.401453(53)		5.438825(83)	
b (Å)	5.427901(50)		5.395555(91)	
c (Å)	7.663798(70)		7.62190(12)	
$\alpha = \gamma$ (deg.)	90.0		90.0	
$\beta$ (deg.)	89.55283(63)		89.9572(19)	
$V$ (Å <sup>3</sup> )	224.6846(37)		223.6682(62)	
	<b>Site-1</b>	<b>Site-2</b>	<b>Site-1</b>	<b>Site-2</b>
Co/Mn-O <sub>1</sub> (Å)	1.87(11)	1.98(12)	2.188(42)	1.683(45)
Co/Mn-O <sub>2</sub> (Å)	1.97(12)	1.89(12)	1.953(90)	1.891(94)
Co/Mn-O <sub>3</sub> (Å)	1.970(73)	1.889(73)	1.799(41)	2.044(41)
d <sub>ave</sub> (Å)	1.937(101)	1.920(104)	1.980(57)	1.873(60)
	<b>Co</b>	<b>Mn</b>	<b>Co</b>	<b>Mn</b>

Table.5-5 Lattice parameters of PrSrCoMnO<sub>6</sub> in T=300 K and T=12 K.

## 5-5 XANES theoretical calculation by XTLS

To confirm the spin state of  $\text{Co}^{3+}$  in  $\text{PrSrCoMnO}_6$ , we also discussed the theoretical calculations of  $L_{2,3}$  XAS line shape by XTLS software from A. Tanaka [8] using the full atomic multiplet theory, together with hybridization of Co 3d orbital with the O 2p ligands and the point charge crystal field in  $\text{CoO}_6$  cluster. The simulation input files were provided by Dr. Z. Hu.

If compare the room temperature  $\text{PrSrCoMnO}_6$  spectrum with the  $\text{Co}^{3+}$  HS and LS spectra more carefully, we find there shows a shoulder characteristic at 777.7 eV in  $\text{PrSrCoMnO}_6$  spectrum, and this characteristic do not come from  $\text{Co}^{3+}$  HS spectra or  $\text{Co}^{3+}$  LS spectra. Compare the 777.7 eV characteristic with CoO spectrum, the shoulder characteristic match well with the first peak of  $L_3$ -edge in CoO, means there exist few oxygen absence at sample surface and cause few presence of  $\text{Co}^{2+}$  ions. To get a pure  $\text{Co}^{3+}$  spectrum, we subtract a suitable ratio of CoO spectrum as shown in Fig. 5-15.

In the simulation of room temperature data, we use the hybridization coefficient  $pd\sigma = -1.70$  eV [4], set  $\Delta e_g = 0$  eV (since distortion doesn't change the  $\text{Co}^{3+}$  spin state). We focus on the peak splitting and ratio of intensity in both  $L_2$  and  $L_3$  edge, a shoulder characteristic in  $L_3$ -edge and a charge transfer characteristic at 788.5 eV. Finally we get a best fit to  $\text{PrSrCoMnO}_6$  spectra in  $10Dq=0.495$  eV (see Fig.5-16).

In the theoretical calculation from XTLS software, the calculation result gives the ground state and first 15 exciting states. For a given temperature parameter, the calculation result spectrum shows the combination from the 16 states and obeys the Boltzmann rule. Table.5-6 shows the energy and total spin  $S(S+1)$  for each state,  $\Delta E$  is the energy difference related to the ground state. The total spectrum considered the thermal excitation at finite temperature. In state-1, the total spin  $S(S+1) = 0.4339917$  presents a low spin state (LS,  $S=0$ ), while the state-2~4 show the  $S(S+1) = 5.983913$

means the total spin is very close to the high spin state (HS,  $S=2$ ).

Fig. 5-17 shows the ground state of several simulations in different fitting parameter  $10Dq$ , and find the ground changes from LS ( $10Dq=0.47259$  eV) to HS ( $10Dq=0.47258$ ). From the Co  $L_2$ -edge XAS spectra line shape, we obviously see that  $\text{PrSrCoMnO}_6$  is neither pure high spin nor pure low spin state

So far, from the list of each state, we assume the cobalt ion is a HS-LS mixed system and can be described as the combination of the ground state (state-1) and the triply degenerate 1<sup>st</sup> exciting state (state-2~4).

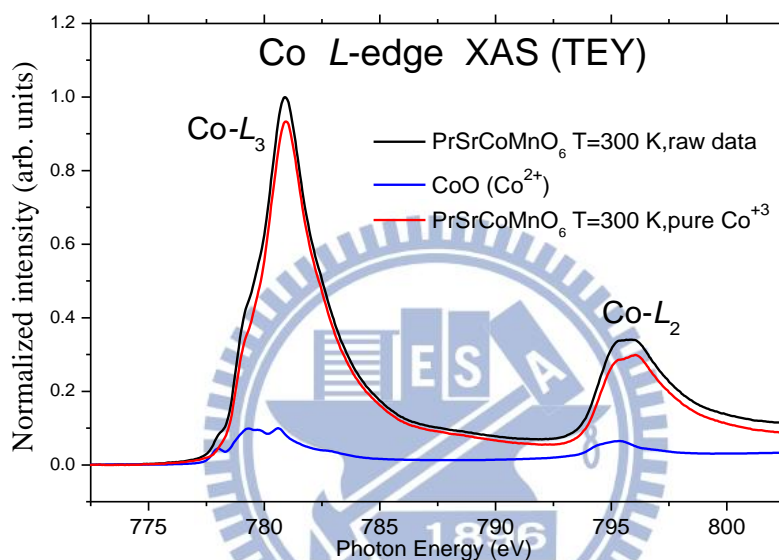


Fig. 5-15 Co  $L$ -edge XAS spectra with  $\text{Co}^{2+}$  impurities

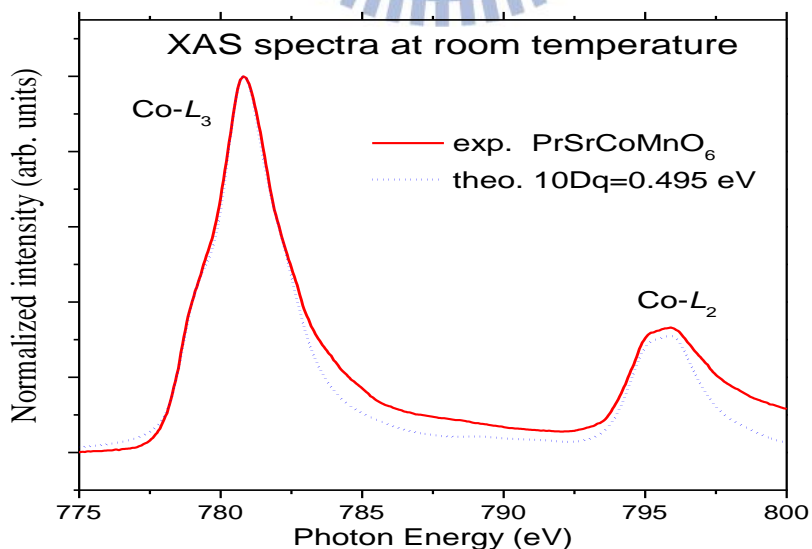


Fig. 5-16 Co  $L$ -edge XAS spectra with theoretical calculation

state	Energy (eV)	S(S+1)	$\Delta E$ (eV)
State-1	-7.8035207919660046	0.4339917	0
State-2	-7.7709324835719755	5.983913	0.032588
State-3	-7.7709324835719746	5.983913	0.032588
State-4	-7.7709324835719746	5.983913	0.032588
State-5	-7.7484215104846887	5.910728	0.055099
State-6	-7.7484215104846879	5.910728	0.055099
State-7	-7.7442833378101614	5.946827	0.059237
State-8	-7.7442833378101605	5.946827	0.059237
State-9	-7.7442833378101597	5.946827	0.059237
State-10	-7.7089677557410514	5.530704	0.094553
State-11	-7.7078332127177269	5.872373	0.095688
State-12	-7.7078332127177269	5.872373	0.095688
State-13	-7.7078332127177269	5.872373	0.095688
State-14	-7.7037092828197791	5.875087	0.099812
State-15	-7.7037092828197808	5.875087	0.099812
State-16	-7.7037092828197800	5.875087	0.099812

Table 5-6 Energy and total spin S(S+1) for each state in  $10Dq=0.495\text{eV}$  by XTLS

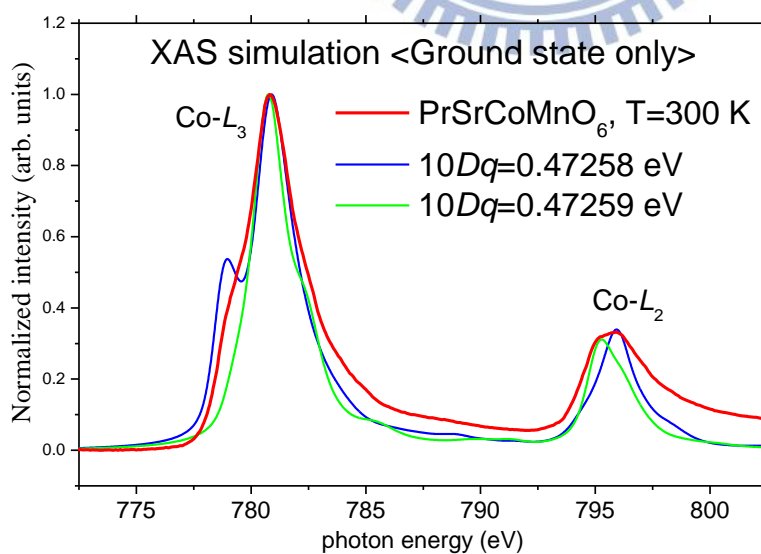


Fig. 5-17 The ground state of simulations in different  $10Dq$

M.W.Haverkort et al.[33] measured Co *L*-edge XAS on LaCoO<sub>3</sub> sample in a wide temperature range and saw the spectra shape changes with temperature in Fig. 5-18. They reveal that LaCoO<sub>3</sub> at finite temperatures is an inhomogeneous mixed-spin state system, and the spin state transition in LaCoO<sub>3</sub> can be well described as a low-spin ground state and a triply degenerate high-spin first excited state. There exist around 25% HS state in room temperature LaCoO<sub>3</sub> spectrum, and the HS population increase with temperature increasing.

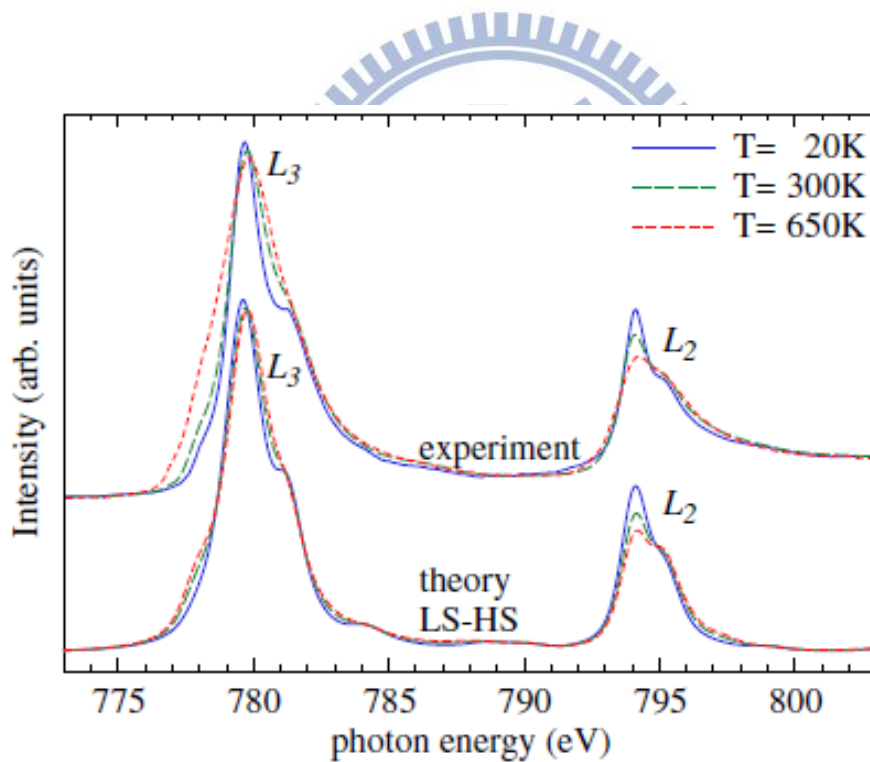


Fig. 5-18 Co *L*-edge XAS in LaCoO<sub>3</sub> from M.W.Haverkort et al.[17]

In the temperature dependent Co *L*-edge XAS experiment of PrSrCoMnO<sub>6</sub>, we also subtract a suitable ratio of CoO spectrum for each spectrum to get a pure Co<sup>3+</sup> spectrum as shown in Fig. 5-19. In the fitting of temperature dependent Co *L*-edge XAS data, we first set the temperature parameter equals to the real experiment condition. We focus on the peak splitting and ratio of intensity in both *L*<sub>2</sub> and *L*<sub>3</sub> edge, a shoulder characteristic in *L*<sub>3</sub>-edge and a charge transfer characteristic at 788.5 eV, finally we found that the 10*Dq*=0.495 eV calculation results can fit both T=300 K and T=400 K data but not for T=18.3 K case. This problem was also mentioned by M.W. Haverkort et al.[33], who studied the spin state transition on LaCoO<sub>3</sub> sample in finite temperature. The best fit to the PrSrCoMnO<sub>6</sub> Co *L*-edge XAS data at T=18.3 K was found at parameter 10*Dq* equals to 0.4743 eV (see Fig. 5-20). The simulation result of 10*Dq*=0.4743 eV also shows a low-spin ground state with the triply degenerate high-spin exciting states. From the calculated energy difference between the LS ground and the HS 1<sup>st</sup> exciting states, together with the Boltzmann rule in finite temperature, our simulations show 39.79% HS population for T=18.3 K, 10*Dq*=0.4743 eV case; 55.70% HS population for T=300 K, 10*Dq*=0.495 eV case; and 67.98% HS for T=400 K, 10*Dq*=0.495 eV case. We obviously see the HS population increases with temperature.

In general case, the crystal size would decrease at low temperature, means the size of CoO<sub>6</sub> octahedral would decrease and the crystal field parameter 10*Dq* should become higher at low temperature, which may not consistent with our calculations. Contrary to the general cases, the powder XRD data of PrSrCoMnO<sub>6</sub> shows an unusual change at low-temperature, the lattice volume and the average Mn-O bond length decrease but the average Co-O bond length increase at low temperature. The longer Co-O bond length may cause a smaller crystal field 10*Dq* in CoO<sub>6</sub> octahedral, which is consistent with our XAS simulation results.



So far, we infer that the cobalt ion in  $\text{PrSrCoMnO}_6$  sample is a HS-LS mixed system, which has a LS ground state and the triply degenerate HS 1<sup>st</sup> exciting states, and the higher HS population, which come from the thermal excitation, presence more at high temperature.

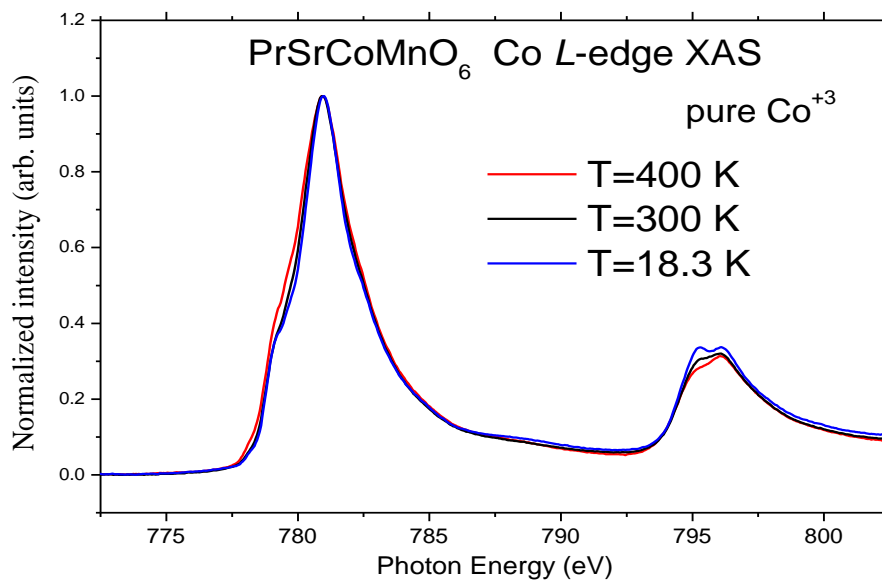


Fig 5-19 Temperature dependent  $\text{Co}^{3+}$  L-edge XAS spectra.

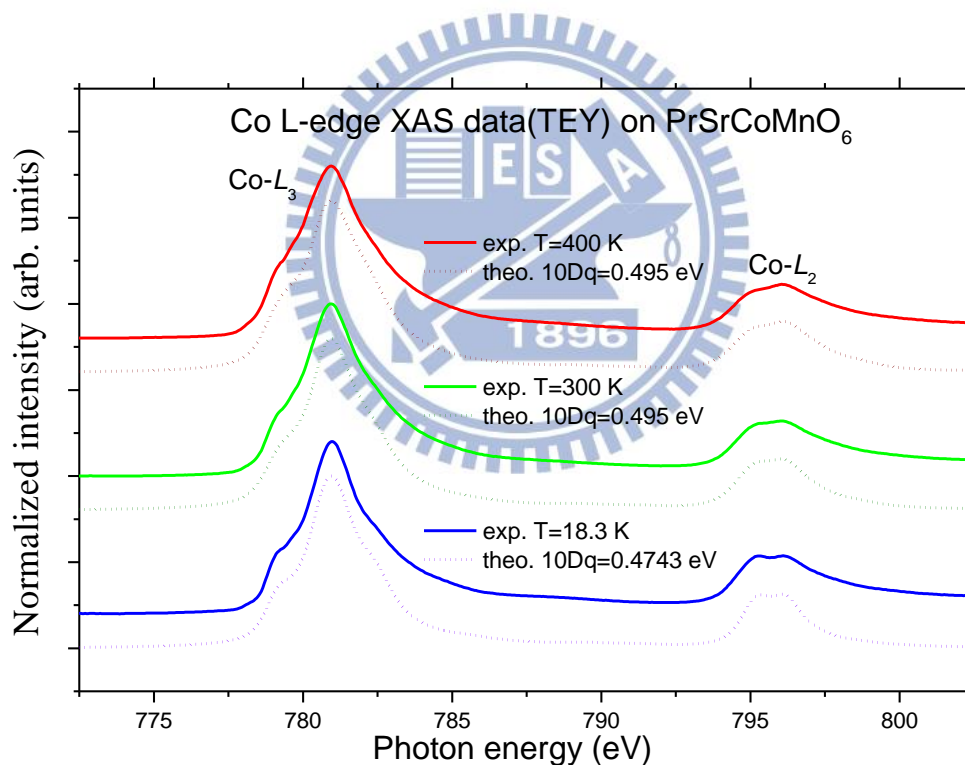


Fig 5-20 Co L-edge XAS experiment data with theoretical calculation (setting the fitting temperature parameter equals to real experiment condition).

At the end, we also fit the room temperature Co L-edge XAS spectra in different samples. The fitting parameter  $10Dq=0.495$  eV shows the best fit to  $\text{PrSrCoMnO}_6$ , while the  $10Dq=0.52$  eV can fit  $\text{LaCoO}_3$  well and  $10Dq=0.54$  eV can fit  $\text{EuCoO}_3$  at room temperature (see Fig.5-21). Compare the average Co-O bond length with the fitting parameter  $10Dq$  in each sample, we obviously see the fitting parameter  $10Dq$  (point charge crystal field in octahedral symmetry) decreasing with the increasing of average Co-O bond length as shown in Fig.5-22. The gray dash curve shows the linear fit of room temperature cases, and the light blue curve shows the  $\text{Co}^{3+}$  ground state HS-LS transition boundary  $10Dq=0.47258$  eV calculated from XTLS software.

Compare with  $\text{EuCoO}_3$  and  $\text{LaCoO}_3$ ,  $\text{PrSrCoMnO}_6$  has the largest average Co-O bond length and the smallest crystal field on  $\text{Co}^{3+}$  ions in the  $\text{CoO}_6$  coordination, and the crystal field in  $\text{PrSrCoMnO}_6$  is much closer to the HS-LS transition boundary, especially in the low temperature.

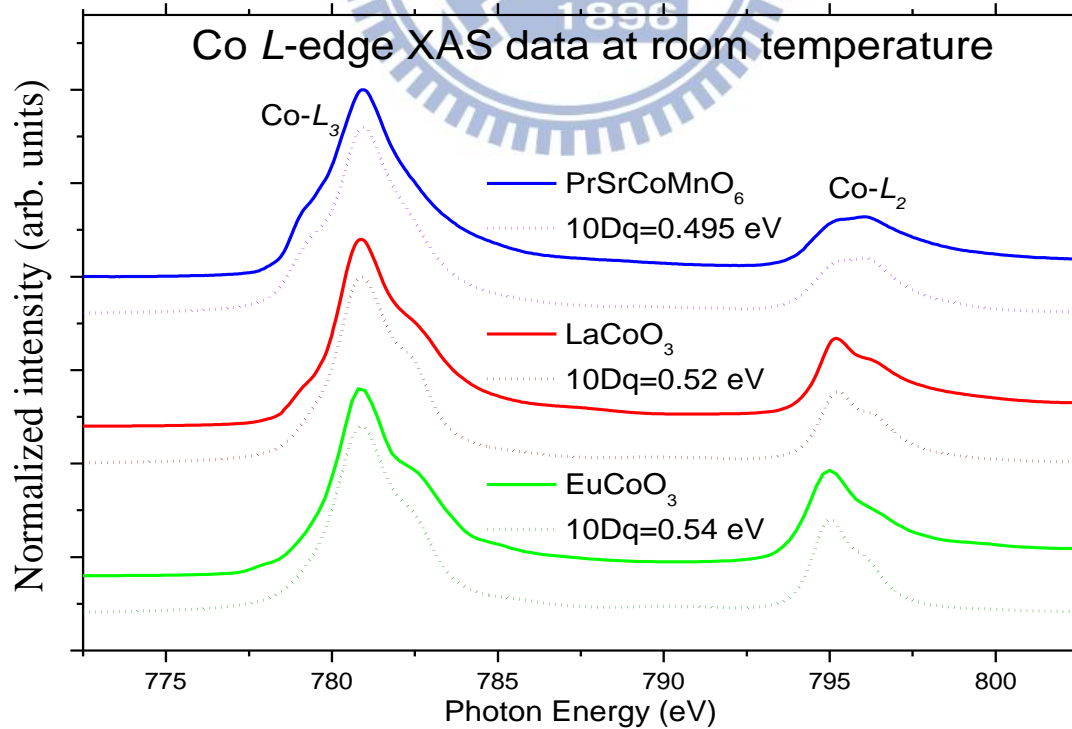


Fig. 5-21 Co L-edge XAS spectra with theoretical calculation

Sample	Average Co-O (Å)	fitting 10Dq (eV)
EuCoO <sub>3</sub>	1.9297	0.54
LaCoO <sub>3</sub>	1.932(1)	0.52
PrSrCoMnO <sub>6</sub> room-T	1.937(101)	0.495
PrSrCoMnO <sub>6</sub> low-T	1.980(57)	0.4743

Table 5-7 The comparison of average Co-O bond length with the fitting parameter

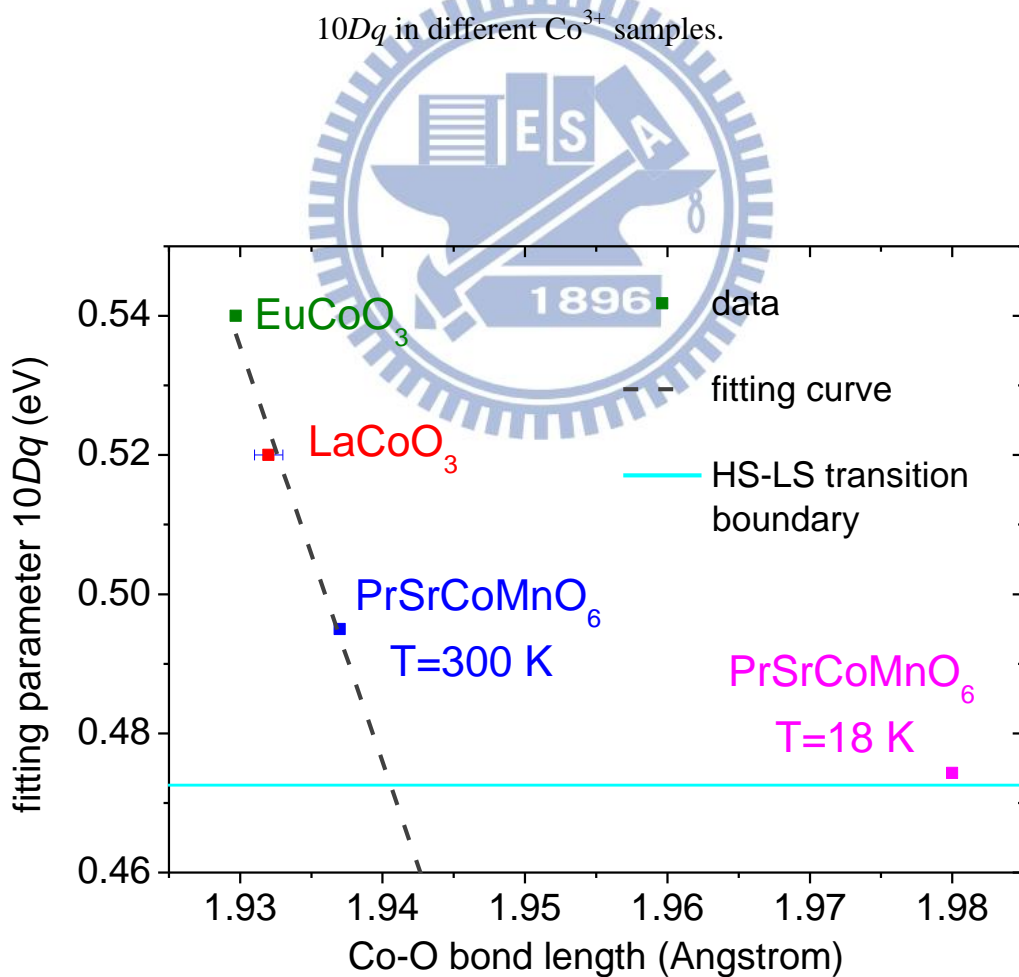


Fig. 5-22 The relationship between the fitting parameter 10Dq with the average Co-O

bond length in different Co<sup>3+</sup> samples.

## Chapter 6. Conclusions and future works

In the Ni *L*-edge XAS experiment on powder Ni(NO<sub>3</sub>)<sub>2</sub> sample, the spectra shows the divalence nickel in Ni(NO<sub>3</sub>)<sub>2</sub> compound. Combine the experiment with the theoretical calculation by XTLS software from A. Tanaka, we assume that the divalence nickel shows a high spin state  $S=1$  in Ni(NO<sub>3</sub>)<sub>2</sub>, same as those nickel ions in NiO, and the different spectra shape between Ni(NO<sub>3</sub>)<sub>2</sub> and NiO come from their different ligand field multiplet effect, which means an undistorted NiO<sub>6</sub> octahedral in NiO and two closely distorted octahedral in Ni(NO<sub>3</sub>)<sub>2</sub>.

In the polycrystal sample PrSrCoMnO<sub>6</sub> experiment using the Co and Mn *K,L*-edge XAS, we infer that the valence state on TM ions is Co<sup>3+</sup>/Mn<sup>4+</sup>, and the cobalt ion in PrSrCoMnO<sub>6</sub> sample is a HS-LS mixed system. Compare with the Co *L*-edge XAS spectra and the crystal structure from X-ray diffraction measurement, we assume the CoO<sub>6</sub> octahedral has a average Co-O bond length 1.937 Å and MnO<sub>6</sub> octahedral has a average Mn-O bond length 1.920 Å in PrSrCoMnO<sub>6</sub> sample at room temperature. PrSrCoMnO<sub>6</sub> shows an unusual change at low temperature, the lattice volume and the average Mn-O bond length decrease, but the average Co-O bond length become longer. From the temperature dependent XAS experiments and the theoretical calculations, which show the crystal field in CoO<sub>6</sub> octahedral of PrSrCoMnO<sub>6</sub> sample is close to the HS-LS transition boundary and the HS population increasing at higher temperature. Combine the XAS spectra, crystal structure and the theoretical calculation from XTLS, we obviously see the relationship between the average Co-O bond length and the crystal field value. We expect to get a larger lattice constant and a longer average Co-O bond length in other  $A'A''B'B''O_6$  Double perovskites compound, which is substituted by other rare earth element or Alkaline earth metal, to see a pure high spin state of Co<sup>3+</sup> ion.

Reference :

- [1] Gerald Giester, Christian L. Lengauer, Manfred Wildner, and Josef Zemann. Z. Kristallogr. 223, 408–417 (2008)
- [2] O. Volkova, E. Deeva, I. Morozov, V. Mazurenko, I. Solovyev, J.-Y. Lin, C.K. Wen, R. Klingeler, B. Büchner, and A. Vasiliev, unpublished
- [3] J. Androulakis, N. Katsarakis, J. Giapintzakis, N. Vouroutzis, E. Pavlidou, K. Chrissafis, E.K. Polychroniadis, and V. Perdikatsis, Journal of Solid State Chemistry 173, 350–354 (2003)
- [4] Z. Hu, Hua Wu, M.W. Haverkort, H. H. Hsieh, H. -J. Lin, T. Lorenz, J. Baier, A. Reichl, I. Bonn, C. Felser, A. Tanaka, C.T. Chen, and L. H. Tjeng, PHYSICAL REVIEW LETTERS, 92, 207402 (2004)
- [5] Grigorii A. Tikhomirov, Konstantin O. Znamenkov, Igor V. Morozov, Erhard Kemnitz, Sergei I. Troyanov, Z. Anorg. Allg. Chem., 628, 269-273 (2002)
- [6] Maria Vallet-Regi, Ester Garcia, and Jose M. Gonzalez-Calbet, J. Chem. Soc. Dalton Trans. (1988)
- [7] N. Vasiliev, O. S. Volkova, L. S. Lobanovskii, I. O. Troyanchuk, Z. Hu, L. H. Tjeng, D. I. Khomskii, H.-J. Lin, C. T. Chen, N. Tristan, F. Kretschmar, R. Klingeler, and B. Büchner, PHYSICAL REVIEW B 77, 104442 (2008).
- [8] Arata Tanaka and Takeo JO, J. Phys. Soc. Jpn. 63, 2788 (1994)
- [9] Maurits W. Haverkort, Universität zu Köln, PHD thesis (2005)
- [10] J.-S. Kang,<sup>1</sup> H. J. Lee, D. H. Kim, S. Kolesnik, B. Dabrowski, K. Świerczek, Jieun Lee, Bongjae Kim, and B. I. Min, PHYSICAL REVIEW B 80, 045115 (2009)
- [11] I. Preda, M. Abbate, A. Gutierrez, S. Palacin, A. Vollmer, and L. Soriano, ELSPEC, 156-158, 111-114 (2007)
- [12] Shie-Ming Peng, Chih-Chieh Wang, Yih-Lih Jang, Yu-Hua Chen, Feng-Yin Li,

- Chung-Yuan Mou, and Man-Kit Leung, *Journal of Magnetism and Magnetic Materials* 209, 80-83(2000)
- [13] M. W. Haverkort, S. I. Csiszar, Z. Hu, S. Altieri, A. Tanaka, H. H. Hsieh, H.-J. Lin, C. T. Chen, T. Hibma, and L. H. Tjeng, *PHYSICAL REVIEW B* 69, 020408 (2004)
- [14] Wenbo Mi, Hua Yang, Yingchun Cheng, and Haili Bai, *Solid State Communications* 152, 1108-1111 (2012)
- [15] Elena Konysheva, Emmanuelle Suard, and John T. S. Irvine, *Chem. Mater.*, 21, 5307–5318 (2009)
- [16] D. Alders, L. H. Tjeng, F. C. Voogt, T. Hibma, G. A. Sawatzky, C. T. Chen, J. Vogel, M. Sacchi, and S. Iacobucci, *PHYSICAL REVIEW B* 57, 11623 (1998)
- [17] J.-S. Kang, S. S. Lee, G. Kim, H. J. Lee, H. K. Song, Y. J. Shin, S. W. Han, C. Hwang, M. C. Jung, H. J. Shin, B. H. Kim, S. K. Kwon, and B. I. Min, *PHYSICAL REVIEW B* 76, 195122 (2007)
- [18] N. Vasiliev, O. S. Volkova, L. S. Lobanovskii, I. O. Troyanchuk, Z. Hu, L. H. Tjeng, D. I. Khomskii, H.-J. Lin, C. T. Chen, N. Tristan, F. Kretzschmar, R. Klingeler, and B. Büchner, *PHYSICAL REVIEW B* 77, 104442 (2008).
- [19] T. Burnus, O. S. Volkova, L. S. Lobanovskii, I. O. Troyanchuk, Z. Hu, L. H. Tjeng, D. I. Khomskii, H.-J. Lin, C. T. Chen, N. Tristan, F. Kretzschmar, R. Klingeler, and B. Büchner, *PHYSICAL REVIEW B* 77, 125124 (2008).
- [20] 高政男，碩士論文，”以吸收光譜研究鈣鈦礦結構中鈷氧化物自旋態與鈷離子價數”，國立交通大學，(2012)。
- [21] C. F. Chang, Z. Hu, HuaWu, T. Burnus, N. Hollmann, M. Benomar, T. Lorenz, A. Tanaka, H.-J. Lin, H. H. Hsieh, C. T. Chen, and L. H. Tjeng, *PHYSICAL REVIEW LETTERS*, 102, 116401 (2009)
- [22] H.-J. Lin, Y. Y. Chin, Z. Hu, G. J. Shu, F. C. Chou, H. Ohta, K. Shimura, S. Hébert,

- A. Maignan, A. Tanaka, L. H. Tjeng, and C. T. Chen, PHYSICAL REVIEW B 81, 115138 (2010)
- [23] J. Prado-Gonjal, A. M. Arevalo-Lopez, E. Morán, Journal of Alloys Compd. (2011) 509, 542-545
- [24] Journal of Physical Chemistry, American Chemical Society (2009) 113, 1250-1251
- [25] Journal of Physics: Condensed Matter (2008) 20, 1452-1452
- [26] Y. Kalyana Lakshmi, P. Venugopal Reddy, Solid State Sciences (2010) 12, 1731-1740
- [27] J. Prado-Gonjal, A. M. Arevalo-Lopez, E. Morán Materials, Research Bulletin 46, 222-230 (2011)
- [28] X. Lan, S. Kong, and W.Y. Zhang, Eur. Phys. J.B. 84, 357-364 (2011)
- [29] I. O. Troyanchuk, A. P. Sazonova, H. Szymczak, D. M. Töbrens, and H. Gamari-Sealed, J. Exp. Theor. Phys, 99, 2, 363-369 (2004)
- [30] Alexander N. Vasiliev, Tatyana M. Vasilchikova, Olga S. Volkova, Anton A. Kamenev, Andrey R. Kaul, Tatyana G. Kuzmova, Dmitry M. Tsybarenko, Kirill A. Lomachenko, Alexander V. Soldatov, Sergey V. Streltsov, Jiunn-Yuan Lin, Cheng-Nan Kao, Jin-Ming Chen, Mahmoud Abdel-Hafiez, Anja Wolter and Rüdiger Klingeler, Journal of the Physical Society of Japan, 82, 044714 (2013)
- [31] J. Peñáz-Cacho, J. Blasco, J. Garcera, and R. Sanchez, solid state Chem, 150, 145 (2000)
- [32] Yang Wang, Yu Sui, Peng Ren, Lan Wang, Xianjie Wang, Wenhui Su, and Hong Jin Fan, Inorg Chem, 49, 3216 (2010)
- [33] M.W. Haverkort, Z. Hu, J. C. Cezar, T. Burnus, H. Hartmann, M. Reuther, C. Zobel, T. Lorenz, A. Tanaka, N. B. Brookes, H. H. Hsieh, H.-J. Lin, C. T. Chen, and L. H. Tjeng, PHYSICAL REVIEW LETTERS, 97, 176405 (2006)